International Journal of Heat and Mass Transfer 52 (2009) 2224–2242

Contents lists available at ScienceDirect

International Journal of Heat and Mass Transfer

journal homepage: www.elsevier.com/locate/ijhmt

# Analysis of mixed convection flows within a square cavity with linearly heated side wall(s)

Tanmay Basak [a], S. Roy [b], Pawan Kumar Sharma [b], I. Pop [c,*]

[a] Department of Chemical Engineering, Indian Institute of Technology Madras, Chennai 600 036, India
[b] Department of Mathematics, Indian Institute of Technology Madras, Chennai 600 036, India
[c] Faculty of Mathematics, University of Cluj, R-3400 Cluj, CP 253, Romania

ARTICLE INFO

*Article history:*
Received 8 May 2008
Received in revised form 30 September 2008
Available online 3 February 2009

*Keywords:*
Mixed convection
Square cavity
Linearly heated side walls

ABSTRACT

Finite element simulations have been performed to investigate the influence of linearly heated side wall(s) or cooled right wall on mixed convection lid-driven flows in a square cavity. It is interesting to note that multiple circulation cells appear inside the cavity with the increase of $Pr$ for $Re = 10$ and $Gr = 10^5$ in the case of linearly heated side walls. For $Pr = 0.015$, only two circulation cells are formed inside the cavity. As $Pr$ increases to 0.7, three circulation cells are formed inside the cavity. Further increase in $Pr$ to 10, leads to the formation of four circulation cells inside the cavity. On the other hand, only two circulation cells are formed inside the cavity for the case of cooled right wall. A detailed analysis of flow pattern shows that as the value of $Re$ increases from 1 to $10^2$, there occurs a transition from natural convection to forced convection depending on the value of $Gr$ irrespective of $Pr$. It is observed that the secondary vortex at the top left corner disappears for $Re = 10^2$ and $Gr = 10^5$ due to enhanced motion of the upper lid in the case of cooled right wall while a small secondary vortex exist at the bottom right corner in the case of linearly heated side walls. The local Nusselt number ($Nu_b$) plot shows that heat transfer rate is equal to 1 at the edges for the case of linearly heated side walls case and that is zero at the left edge and thereafter that increases for the case of cooled right wall. It is interesting to observe that $Nu_b$ is large within $0.4 \leqslant X \leqslant 0.6$ due to compression of isotherms for $Pr = 0.7$ and 10 in the case of linearly heated side wall. It is also observed that $Nu_r$ or $Nu_l$ exhibits oscillations especially for $Pr = 10$ at higher $Gr$ due to the presence of multiple circulations. It is also observed that $\overline{Nu_r}$ or $\overline{Nu_l}$ vs $Gr$ plots show oscillation for two case studies. Average Nusselt numbers at the bottom and right walls are strong functions of Grashof number at larger Prandtl numbers whereas average Nusselt number at the left wall at a specific $Pr$ is a weaker function of $Gr$.

© 2009 Elsevier Ltd. All rights reserved.

## 1. Introduction

Recent technological implications have given rise to increased interest in combined free, forced and mixed convection flows in channels, ducts and cavities in which the objective is to secure a quantitative understanding of a configuration having current engineering application. Mixed convection flow in channels, ducts and cavities may occur in many applications, such as in heat exchangers, ventilation of rooms, double glazing, nuclear reactor insulation, solar energy collection, chemical processing equipment, microelectronic cooling, crystal growth in liquids, to name just a few of these applications [1]. Further, mixed convection problems with lid-driven flows in an enclosure finds a wide range of applications in various fields of engineering and science such as flow and heat transfer in solar ponds [2], dynamics of lakes [3], thermal-hydraulics of nuclear reactors [4], food processing and float glass production [5]. The determination of buoyancy-driven flow in cavities is also an interesting problem for evaluating the performance of numerical methods dealing with viscous flow calculations. The lid-driven cavity problem has been extensively used as a benchmark case for the evaluation of numerical solution algorithms [6,7].

The governing non-dimensional parameters used here for the description of flows are Grashof number ($Gr$), Reynolds number ($Re$) and Prandtl number ($Pr$). Another dimensionless parameter, Richardson number ($Ri = Gr/Re^n$), also arises from the Boussinesq approximation for the analysis of mixed convection. Analysis indicates that Richardson number ($Ri$) characterizes mixed convection flow where the Grashof number ($Gr$) and Reynolds number ($Re$) represent the strength of the natural and forced convection flow effects, respectively. The limiting case $Ri \to 0$ and $Ri \to \infty$ correspond to the forced and natural convection flows, respectively. The exponent $n$ depends on the geometry, thermal boundary

* Corresponding author.
*E-mail addresses:* tanmay@iitm.ac.in (T. Basak), sjroy@iitm.ac.in (S. Roy), pop.ioan@yahoo.co.uk (I. Pop).

0017-9310/$ - see front matter © 2009 Elsevier Ltd. All rights reserved.
doi:10.1016/j.ijheatmasstransfer.2008.10.033

**Nomenclature**

| | |
|---|---|
| $g$ | acceleration due to gravity, ms$^{-2}$ |
| $Gr$ | Grashof number |
| $J$ | Jacobian of residual equations |
| $k$ | thermal conductivity,W m$^{-1}$ K$^{-1}$ |
| $L$ | height of the square cavity, m |
| $N$ | total number of nodes |
| $Nu$ | local Nusselt number |
| $\overline{Nu}$ | average Nusselt number |
| $p$ | pressure, Pa |
| $P$ | dimensionless pressure |
| $Pe$ | Peclet number |
| $Pr$ | Prandtl number |
| $R$ | residual of weak form |
| $Re$ | Reynolds number |
| $Ri$ | Richardson number |
| $T$ | temperature, K |
| $T_h$ | temperature of hot bottom wall, K |
| $T_c$ | temperature of cold wall, K |
| $u$ | $x$ component of velocity, m s$^{-1}$ |
| $U$ | $x$ component of dimensionless velocity |
| $v$ | $y$ component of velocity, m s$^{-1}$ |
| $V$ | $y$ component of dimensionless velocity |
| $X$ | dimensionless distance along $x$ coordinate |
| $Y$ | dimensionless distance along $y$ coordinate |

*Greek symbols*

| | |
|---|---|
| $\alpha$ | thermal diffusivity, m$^2$ s$^{-1}$ |
| $\beta$ | volume expansion coefficient, K$^{-1}$ |
| $\gamma$ | penalty parameter |
| $\theta$ | dimensionless temperature |
| $\nu$ | kinematic viscosity, m$^2$ s$^{-1}$ |
| $\rho$ | density, kg m$^{-3}$ |
| $\Phi$ | basis functions |
| $\psi$ | stream function |

*Subscripts*

| | |
|---|---|
| $b$ | bottom wall |
| $i$ | residual number |
| $k$ | node number |
| $s$ | side wall |

*Superscript*

| | |
|---|---|
| $n$ | Newton iterative index |

condition and the fluid. The limiting conditions based on $Ri$ are not invariant for any Prandtl number ($Pr$) or Peclet number ($Pe$) and flow and temperature characteristics are uniquely determined for fixed $Pr$ or $Pe$, $Re$ and $Gr$. The two sets of parameters may determine the flow and temperature characteristics based on either (i) $Re, Pr$ and $Gr$ or (ii) $Re, Pe$ and $Ri$. The first set of parameters is commonly used in analysis for mixed convection in various applications [8]. Bejan [9] carried out a scale analysis of mixed convection flow over a vertical wall and showed that the criterion for the transition from the forced convection dominant flow to natural convection dominant flow was not the same for fluids with $Pr \geqslant 1$ and $Pr \leqslant 1$. The transition criterion is not yet validated for $Pr \ll 1$ due to non existence of experimental data for this range of $Pr$.

Previous studies reflect that there are two categories of study available for mixed convection flows in enclosures. The first category is concerned with a horizontal sliding lid which encompasses the top wall [10–14], bottom sliding wall [15,16] or an oscillating lid [17,18]. These studies have been extended for three-dimensional cavities [19,20]. The other type of problem is associated with side driven differentially heated enclosures, where one wall or both vertical walls move with a constant velocity in their planes [21–23]. Moallemi and Jang [10] analyzed the effects of Prandtl number ($Pr$) on laminar mixed convection heat transfer in a lid-driven cavity. They performed the numerical simulations for two-dimensional laminar flow ($100 \leqslant Re \leqslant 2200$) and studied the effects of small to moderate Prandtl numbers ($0.01 \leqslant Pr \leqslant 50$) on the flow and heat transfer in a square cavity for various values of Richardson number, $Ri$. The temperature and flow fields in the cavity are calculated and presented to illustrate the strong influence of Prandtl number, $Pr$. The local and average Nusselt numbers are also reported for various values of $Re, Ri$ and $Pr$. Mixed convection heat transfer in a lid-driven cavity was also investigated by Prasad and Koseff [11]. They performed a series of experiments in a cavity filled with water and measured heat flux at various locations over the hot cavity floor for a range of $Re$ and $Gr$. Their results indicate that the overall (i.e. area averaged) heat transfer rate was very weak function of $Gr$ for the range of $Re$ examined ($2200 \leqslant Re \leqslant 12,000$).

A detailed analysis on the stability of mixed convection has been carried out by Mohamad and Viskanta [12] and they reported on the onset of instability in a shallow lid-driven cavity heated from below. They carried out a linear stability analysis and found that $Pr$ influences the conditions for the initiation of the mixed convection regime. Analysis of mixed convection has been studied for various applications. Amiri et al. [13] have analyzed the effects of mixed convection heat transfer in lid-driven cavity with sinusoidal wavy bottom surface. They investigated the implications of Richardson number ($Ri$), number of wavy surface undulations, and amplitude of wavy surface on the flow structure for $Pr = 1$. They have also illustrated that the average Nusselt number increases with an increase in both amplitude of the wavy surface and Reynolds number ($Re$).

Mohamad and Viskanta [14] analyzed convective motion and heat transfer in a square cavity driven by combined temperature gradient and imposed lid shear for low Prandtl number fluid ($Pr = 0.005$). They reported that for $Gr/Re^2 \geqslant 1$ the effect of inertia is insignificant and for $Gr/Re^2 \leqslant 1$ the inertia stabilizes the flow, regardless of the direction of the applied shear force. Iwatsu et al. [18] numerically studied the effect of oscillating lid for a viscous thermally stratified fluid in a square container. Iwatsu and Hyun [19] also carried three-dimensional numerical simulations of fluid flow and heat transfer in a lid-driven cavity and analyzed the result for different values of $Ri$ and $Pr = 0.71$. They observed that when $Ri \geqslant O(1)$, the stable temperature distribution tends to suppress the vertical fluid motion and as a result much of the fluid motion takes place in the vicinity of the top sliding lid and the bulk of the cavity region is nearly stagnant. Oztop and Dagtekin [23] studied steady state two-dimensional mixed convection problem in a vertical two-sided lid-driven differentially heated square cavity. They observed that both Richardson number and direction of moving walls affect the fluid flow and heat transfer in the cavity. For $Ri \leqslant 1$, the influence of moving walls on the heat transfer is the same when the walls move in opposite direction regardless of which side moving upwards and the influence is less when both sides move upwards. For the case of opposing buoyancy and shear forces and for $Ri \geqslant 1$, the heat transfer rate is larger due to formation of secondary cells on the walls and a counter rotating cell at the center.

Mixed convection studies are also carried out in presence of isolated or discrete heat sources [24–26]. Papanicolaou and Jaluria

[24] studied the effects of mixed convection from an isolated heat source in a rectangular enclosure. Their study is based on the mixed convection transport from an isolated thermal source, with a uniform surface heat flux input and located in a rectangular enclosure. The objective of the work is to analyze the interaction of the cooling stream with the buoyancy-induced flow from the heat source. Hsu et al. [25] studied combined free and forced convection in a partially divided enclosure with a finite-size heat source. The enclosure is partially divided by a conductive vertical divider protruding from the floor or the ceiling of the enclosure. The present study simulates a practical system such as air-cooled electronic equipment with heated components. The results indicate that the average Nusselt number and the dimensionless surface temperature on the heat source strongly depend on the location and the height of the divider. Hsu and Wang [26] carried out numerical study on mixed convective heat transfer in rectangular enclosure. The discrete heat sources are embedded on a vertical board, which is situated on the bottom wall of an enclosure. An external airflow enters the enclosure through an opening in one vertical wall and exits from another opening in the opposite wall. The computational results indicate that both the thermal field and the average Nusselt number ($\overline{Nu}$) depend strongly on the governing parameters, position of the heat sources, as well as the property of the heat-source-embedded board. Although there are a number of studies available in the literature as mentioned above for mixed convection flows within enclosures, but the detailed analysis on heat and fluid flow for uniform and non-uniform heating cases with local and average heat transfer rates as a function of various governing parameters is yet to appear in the literature.

Current study deals with the mixed convection heating of commonly used liquids in a square enclosure where the bottom wall is heated uniformly, left vertical wall is heated linearly, right vertical wall is either linearly heated or cooled and the insulated top wall is sliding with a uniform velocity. These boundary conditions are typical representations of heating of fluid in a container where heat treatment is applied at the bottom and the side wall would correspond to linear heating rate such that the heating rate is zero at the top of the side wall. The cold side wall often appears in presence of cold outer environment and this cold side wall may also cause locally larger thermal gradient. Convection patterns in such situation may be interesting and the studies on mixed convection with such boundary conditions are not yet reported till date. The aim of the present investigation is to provide a complete understanding about the physical insight of the problem, solution procedure using finite element method and detailed analysis of temperature and the flow fields on heat transfer evaluation. The geometry of square cavity with boundary conditions is shown in Fig. 1. In the current study, Galerkin finite element [27] method has been used with penalty parameter to solve the nonlinear coupled partial differential equations governing flow and temperature fields. The detailed analysis of heat transfer rates or Nusselt numbers has been carried out using finite element basis functions.

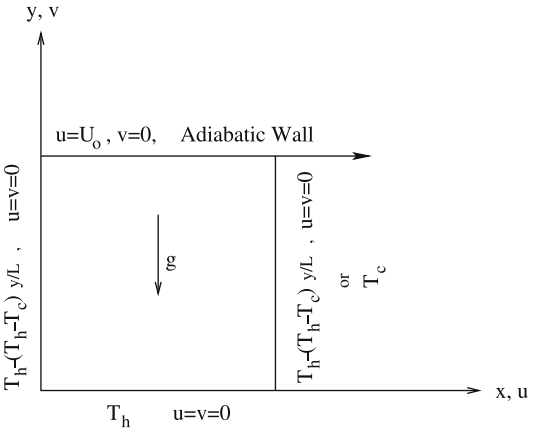


**Fig. 1.** Schematic diagram of the physical system.

## 2. Problem formulation

A two-dimensional square cavity is considered for the present study with the physical dimensions as shown in the Fig. 1. The bottom wall of the cavity is maintained at a uniform temperature and the top wall is insulated. The left vertical wall is heated linearly and the right vertical wall is either heated linearly or maintained at cold temperature. The bottom wall is maintained at a higher temperature to induce buoyancy effect. The top wall is assumed to slide from left to right with a constant speed $U_0$. The flow is assumed to be laminar and the fluid properties are assumed to be constant except for the density variation which is treated according to Boussinesq approximation while viscous dissipation effects are considered to be negligible. The governing equations for the viscous incompressible flow and the temperature distribution inside the cavity are the Navier–Stokes equations and the energy equations, respectively. The governing equations are non-dimensionalized to yield

$$\frac{\partial U}{\partial X}+\frac{\partial V}{\partial Y}=0, \tag{1}$$

$$U\frac{\partial U}{\partial X}+V\frac{\partial U}{\partial Y}=-\frac{\partial P}{\partial X}+\frac{1}{Re}\left(\frac{\partial^2 U}{\partial X^2}+\frac{\partial^2 U}{\partial Y^2}\right), \tag{2}$$

$$U\frac{\partial V}{\partial X}+V\frac{\partial V}{\partial Y}=-\frac{\partial P}{\partial Y}+\frac{1}{Re}\left(\frac{\partial^2 V}{\partial X^2}+\frac{\partial^2 V}{\partial Y^2}\right)+\frac{Gr}{Re^2}\theta, \tag{3}$$

$$U\frac{\partial \theta}{\partial X}+V\frac{\partial \theta}{\partial Y}=\frac{1}{RePr}\left(\frac{\partial^2 \theta}{\partial X^2}+\frac{\partial^2 \theta}{\partial Y^2}\right). \tag{4}$$

The transformations of variables in order to obtain dimensionless governing equations are given as follows:

$$\begin{aligned}&U(X,1)=1,\quad U(X,0)=U(0,Y)=U(1,Y)=0,\\&V(X,0)=V(X,1)=V(0,Y)=V(1,Y)=0,\\&\theta(X,0)=1,\quad \frac{\partial\theta}{\partial Y}(X,1)=0,\\&\theta(0,Y)=1-Y,\quad \theta(1,Y)=1-Y \text{ or } 0.\end{aligned} \tag{5}$$

The transformations used are as follows:

$$\begin{aligned}&X=\frac{x}{L},\quad Y=\frac{y}{L},\quad U=\frac{u}{U_0},\quad V=\frac{v}{U_0},\quad \theta=\frac{T-T_c}{T_h-T_c},\\&P=\frac{p}{\rho U_0^2},\quad Pr=\frac{\nu}{\alpha},\quad Re=\frac{U_0 L}{\nu},\quad Gr=\frac{g\beta(T_h-T_c)L^3}{\nu^2}.\end{aligned} \tag{6}$$

Here $x$ and $y$ are the distances measured along the horizontal and vertical directions, respectively; $u$ and $v$ are the velocity components in the $x$ and $y$ directions, respectively; $T$ denotes the temperature; $p$ is the pressure and $\rho$ is the density; $T_h$ and $T_c$ are the temperature at the hot and cold walls, respectively; $L$ is the length of the side of the square cavity; $X$ and $Y$ are dimensionless coordinates varying along horizontal and vertical directions, respectively; $U_0$ is the velocity of the upper wall; $U$ and $V$ are dimensionless velocity components in the $X$ and $Y$ directions, respectively; $\theta$ is the dimensionless temperature; $P$ is the dimensionless pressure; $Gr, Re$ and $Pr$ are Grashof, Reynolds and Prandtl numbers, respectively.

## 3. Solution procedure

The momentum and energy balance equations [Eqs. (2)–(4)] which are elliptic system of equations have been solved using

the Galerkin finite element method. The continuity equation [Eq. (1)] will be used as a constraint due to mass conservation and this constraint may be used to obtain the pressure distribution. In order to solve Eqs. (2–3), we use the penalty finite element method where the pressure $P$ is eliminated by a penalty parameter ($\gamma$) and the incompressibility criteria given by Eq. (1) [27] results in

$$P = -\gamma\left(\frac{\partial U}{\partial X}+\frac{\partial V}{\partial Y}\right). \tag{7}$$

The continuity equation [Eq. (1)] is automatically satisfied for large values of $\gamma$. Typical values of $\gamma$ that yield consistent solutions are $10^7$. Using Eq. (7), the momentum balance equations [Eqs. (2) and (3)] reduce to

$$U\frac{\partial U}{\partial X}+V\frac{\partial U}{\partial Y}=\gamma\frac{\partial}{\partial X}\left(\frac{\partial U}{\partial X}+\frac{\partial V}{\partial Y}\right)+\frac{1}{Re}\left(\frac{\partial^2 U}{\partial X^2}+\frac{\partial^2 U}{\partial Y^2}\right), \tag{8}$$

and

$$U\frac{\partial V}{\partial X}+V\frac{\partial V}{\partial Y}=\gamma\frac{\partial}{\partial Y}\left(\frac{\partial U}{\partial X}+\frac{\partial V}{\partial Y}\right)+\frac{1}{Re}\left(\frac{\partial^2 V}{\partial X^2}+\frac{\partial^2 V}{\partial Y^2}\right)+\frac{Gr}{Re^2}\theta. \tag{9}$$

The system of equations [Eqs. (4), (8) and (9)] with boundary conditions [Eq. (5)] are solved by using Galerkin finite element method [27]. Expanding the velocity components $(U, V)$ and temperature $(\theta)$ using basis set $\{\Phi_k\}_{k=1}^N$ as,

$$U\approx\sum_{k=1}^{N}U_k\Phi_k(X,Y),\quad V\approx\sum_{k=1}^{N}V_k\Phi_k(X,Y)\quad\text{and}\quad\theta\approx\sum_{k=1}^{N}\theta_k\Phi_k(X,Y) \tag{10}$$

the Galerkin finite element method yields the following nonlinear residual equations for Eqs. (8), (9) and (4), respectively, at nodes of internal domain $\Omega$:

$$\begin{aligned}R_i^{(1)}=&\sum_{k=1}^{N}U_k\int_\Omega\left[\left(\sum_{k=1}^{N}U_k\Phi_k\right)\frac{\partial\Phi_k}{\partial X}+\left(\sum_{k=1}^{N}V_k\Phi_k\right)\frac{\partial\Phi_k}{\partial Y}\right]\Phi_i dXdY\\&+\gamma\left[\sum_{k=1}^{N}U_k\int_\Omega\frac{\partial\Phi_i}{\partial X}\frac{\partial\Phi_k}{\partial X}dXdY+\sum_{k=1}^{N}V_k\int_\Omega\frac{\partial\Phi_i}{\partial X}\frac{\partial\Phi_k}{\partial Y}dXdY\right]\\&+\frac{1}{Re}\sum_{k=1}^{N}U_k\int_\Omega\left[\frac{\partial\Phi_i}{\partial X}\frac{\partial\Phi_k}{\partial X}+\frac{\partial\Phi_i}{\partial Y}\frac{\partial\Phi_k}{\partial Y}\right]dXdY\end{aligned} \tag{11}$$

$$\begin{aligned}R_i^{(2)}=&\sum_{k=1}^{N}V_k\int_\Omega\left[\left(\sum_{k=1}^{N}U_k\Phi_k\right)\frac{\partial\Phi_k}{\partial X}+\left(\sum_{k=1}^{N}V_k\Phi_k\right)\frac{\partial\Phi_k}{\partial Y}\right]\Phi_i dXdY\\&+\gamma\left[\sum_{k=1}^{N}U_k\int_\Omega\frac{\partial\Phi_i}{\partial Y}\frac{\partial\Phi_k}{\partial X}dXdY+\sum_{k=1}^{N}V_k\int_\Omega\frac{\partial\Phi_i}{\partial Y}\frac{\partial\Phi_k}{\partial Y}dXdY\right]\\&+\frac{1}{Re}\sum_{k=1}^{N}V_k\int_\Omega\left[\frac{\partial\Phi_i}{\partial X}\frac{\partial\Phi_k}{\partial X}+\frac{\partial\Phi_i}{\partial Y}\frac{\partial\Phi_k}{\partial Y}\right]dXdY\\&-\frac{Gr}{Re^2}\int_\Omega\left(\sum_{k=1}^{N}\theta_k\Phi_k\right)\Phi_i dXdY\end{aligned} \tag{12}$$

and

$$\begin{aligned}R_i^{(3)}=&\sum_{k=1}^{N}\theta_k\int_\Omega\left[\left(\sum_{k=1}^{N}U_k\Phi_k\right)\frac{\partial\Phi_k}{\partial X}+\left(\sum_{k=1}^{N}V_k\Phi_k\right)\frac{\partial\Phi_k}{\partial Y}\right]\Phi_i dXdY\\&+\frac{1}{RePr}\sum_{k=1}^{N}\theta_k\int_\Omega\left[\frac{\partial\Phi_i}{\partial X}\frac{\partial\Phi_k}{\partial X}+\frac{\partial\Phi_i}{\partial Y}\frac{\partial\Phi_k}{\partial Y}\right]dXdY.\end{aligned} \tag{13}$$

The set of non-linear algebraic equations [Eqs. (12 and 13)] are solved using reduced integration technique [28] and Newton Raphson method as discussed in earlier work [29,30]. At each iteration, the linear $(3N\times 3N)$ system;

$$\mathbf{J}(\mathbf{a}^n)[\mathbf{a}^n-\mathbf{a}^{n+1}]=\mathbf{R}(\mathbf{a}^n), \tag{14}$$

is solved where $n$ is the iterative index. The elements of the Jacobian matrix, $\mathbf{J}(\mathbf{a}^n)$ contains the derivatives of the residual equations with respect to velocity components $(U_j)$'s, $(V_j)$'s and the temperature $(\theta_j$'s) and $\mathbf{R}(\mathbf{a}^n)$ is the vector of residuals. The linear system for each iteration is based on efficient node numbering of the elements such that the jacobian forms a banded matrix. The iterative process is terminated with the convergence criterion $\left[\sum(R_i^{(j)})^2\right]^{0.5}\leqslant 10^{-5}$ using two-norm of residual vectors.

The numerical solutions are obtained in terms of the velocity components $(U, V)$ and stream function $(\psi)$ is evaluated using the relationship between the stream function $(\psi)$ and the velocity components [31], where the stream function $(\psi)$ is defined in the usual way as $U=\partial\psi/\partial Y$ and $V=-\partial\psi/\partial X$. It may be noted that, the positive sign of $\psi$ denotes anti-clockwise circulation and the clockwise circulation is represented by the negative sign of $\psi$. The no-slip condition is valid at all boundaries as there is no cross flow, hence $\psi=0$ is used for the boundaries. The heat transfer coefficient in terms of the local Nusselt number $(Nu)$ is defined by

$$Nu=-\frac{\partial\theta}{\partial n}, \tag{15}$$

where $n$ denotes the normal direction on a plane. The local Nusselt numbers at bottom wall $(Nu_b)$ and at the side wall $(Nu_s)$ are defined as:

$$Nu_b=-\sum_{i=1}^{9}\theta_i\frac{\partial\Phi_i}{\partial Y} \tag{16}$$

and

$$Nu_s=-\sum_{i=1}^{9}\theta_i\frac{\partial\Phi_i}{\partial X}. \tag{17}$$

The average Nusselt numbers at the bottom and side walls are:

$$\overline{Nu_b}=\frac{\int_0^1 Nu_b dX}{X|_0^1}=\int_0^1 Nu_b dX \tag{18}$$

and

$$\overline{Nu_s}=\frac{\int_0^1 Nu_s dY}{Y|_0^1}=\int_0^1 Nu_s dY \tag{19}$$

Note that, $Nu_s$ may be denoted as $Nu_l$ and $Nu_r$ for the left and right walls, respectively.

## 4. Results and discussion

### 4.1. Numerical tests

The computational domain consists of $28\times 28$ bi-quadratic elements which correspond to $57\times 57$ grid points. The bi-quadratic elements with lesser number of nodes smoothly capture the nonlinear variations of the field variables which are in contrast with finite difference/finite volume solution available in the literature [23,10]. Fig. 2a and b shows streamlines and isotherms for the fluid confined within hot bottom and top cold walls with insulated side walls and the results are in good agreement with the earlier work [10]. Fig. 3a–c illustrate the influence of number of grid points for a test case of fluid confined within cavity subjected to uniform heating of bottom wall with linearly heated side walls in presence of top adiabatic wall. The simulation results are shown for $49\times 49$ (Fig. 3a), $57\times 57$ (Fig. 3b) and $61\times 61$ grid points (Fig. 3c). It is found that temperature and flow characteristics with $57\times 57$ and $61\times 61$ grids are identical and further simulation studies are performed based on $57\times 57$ grids.

Numerical solutions are obtained for $Gr=10^3-10^5$, $Pr=0.015-10$ and $Re=1-10^2$ with uniform heating of the bot-

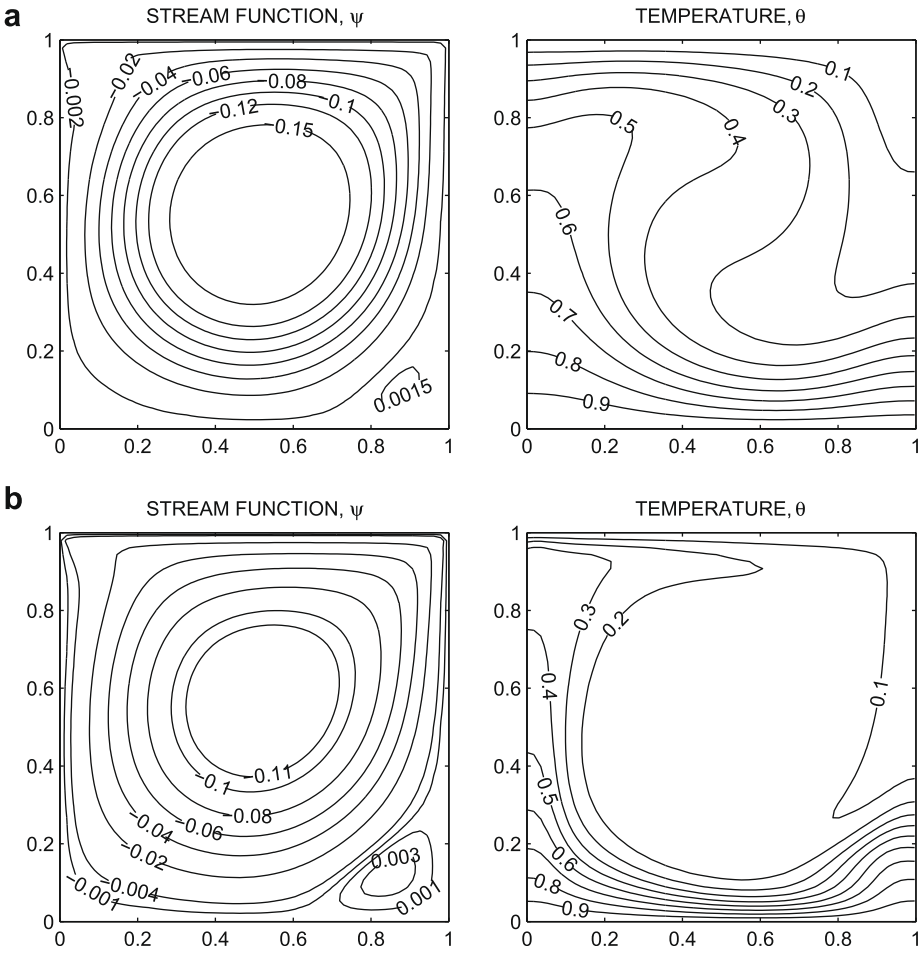


**Fig. 2.** Benchmark results of stream function and temperature contours for fluid confined within cold top and hot bottom wall with insulated side walls [10] for (a) $Pr = 0.1,\ Re = 500,\ Gr = 10^5$ and (b) $Pr = 1,\ Re = 500,\ Gr = 10^5$. The results are shown for $57 \times 57$ grid points.

tom wall where the two vertical walls are linearly heated or the right wall is kept at cold temperature and the top wall is well insulated with a horizontal velocity $U = 1$. In case of cold right wall, the jump discontinuity due to Dirichlet type boundary condition at the corner point (see Fig. 1) corresponds to computational singularity. The convergence tests for the particular situation is carried out in following manner. The grid size dependent effect of the temperature discontinuity at the corner points upon the local (and the overall) Nusselt numbers tend to increase as the mesh spacing at the corner is reduced. One of the ways for handling the problem is assuming the average temperature of the two walls at the corner and keeping the adjacent grid-nodes at the respective wall temperatures. Alternatively, based on earlier work by Ganzarolli and Milanez [32], this procedure is still grid dependent unless a sufficiently refined mesh is implemented. Accordingly, once any corner formed by the intersection of two differentially heated boundary walls is assumed at the average temperature of the adjacent walls, the optimal grid size obtained for each configuration corresponds to the mesh spacing over which further grid refinements lead to grid invariant results in both heat transfer rates and flow fields.

In the current investigation, Gaussian quadrature based finite element method provides the smooth solutions at the interior domain including the corner region as evaluation of residual depends on interior Gauss points and thus the effect of corner node is less pronounced in the final solution. The present finite element approach offers special advantage on evaluation of local Nusselt number at the bottom and side walls as the element basis functions are used to evaluate the heat flux.

### *4.2. Effect of Grashof number (Gr) for linearly heated side walls or with cooled right wall*

Figs. 4–7 display the stream function and isotherm contours of the numerical results for $Gr = 10^3 - 10^5, Pr = 0.015 - 10$ with $Re = 10$ when the side walls are linearly heated or the left wall linearly heated with cooled right wall whereas the bottom wall is maintained at uniform heating. Fig. 4a shows that for $Gr = 10^3$, the effect of lid-driven flow predominates the natural convection. The lid velocity produces inertia effect on the flow near the upper boundary. Due to strong inertial effects produced by the motion of the upper wall, secondary circulation does not appear inside the cavity for $Gr = 10^3$. Overall, flow scenario resembles the case of lid-driven flow and the circulation is stronger at the core of the cavity. At $Gr = 10^4$, both primary and secondary circulations are formed inside the cavity (see Fig. 4b). It is interesting to note that due to the increase in $Gr$, the significant effect of buoyancy results in an onset of natural convection flow at the left corner of the bottom wall. A small amount of fluid is dragged from the core along with the rising fluids from the left half of the cavity due to the increased strength of buoyancy and secondary circulation with anticlockwise rotation is observed. The strength of clockwise circulation is stronger as compared to the anticlockwise circulation for $Gr = 10^4$. In fact, the major portion of the cavity is occupied by primary clockwise circulation and the secondary anticlockwise circulation occupies a small portion near the left side wall. At $Gr = 10^5$, the natural convection becomes equally dominant as the lid-driven flow and the strength of both the circulations are increased. Due to uniform heating of the bottom wall, fluids rise from

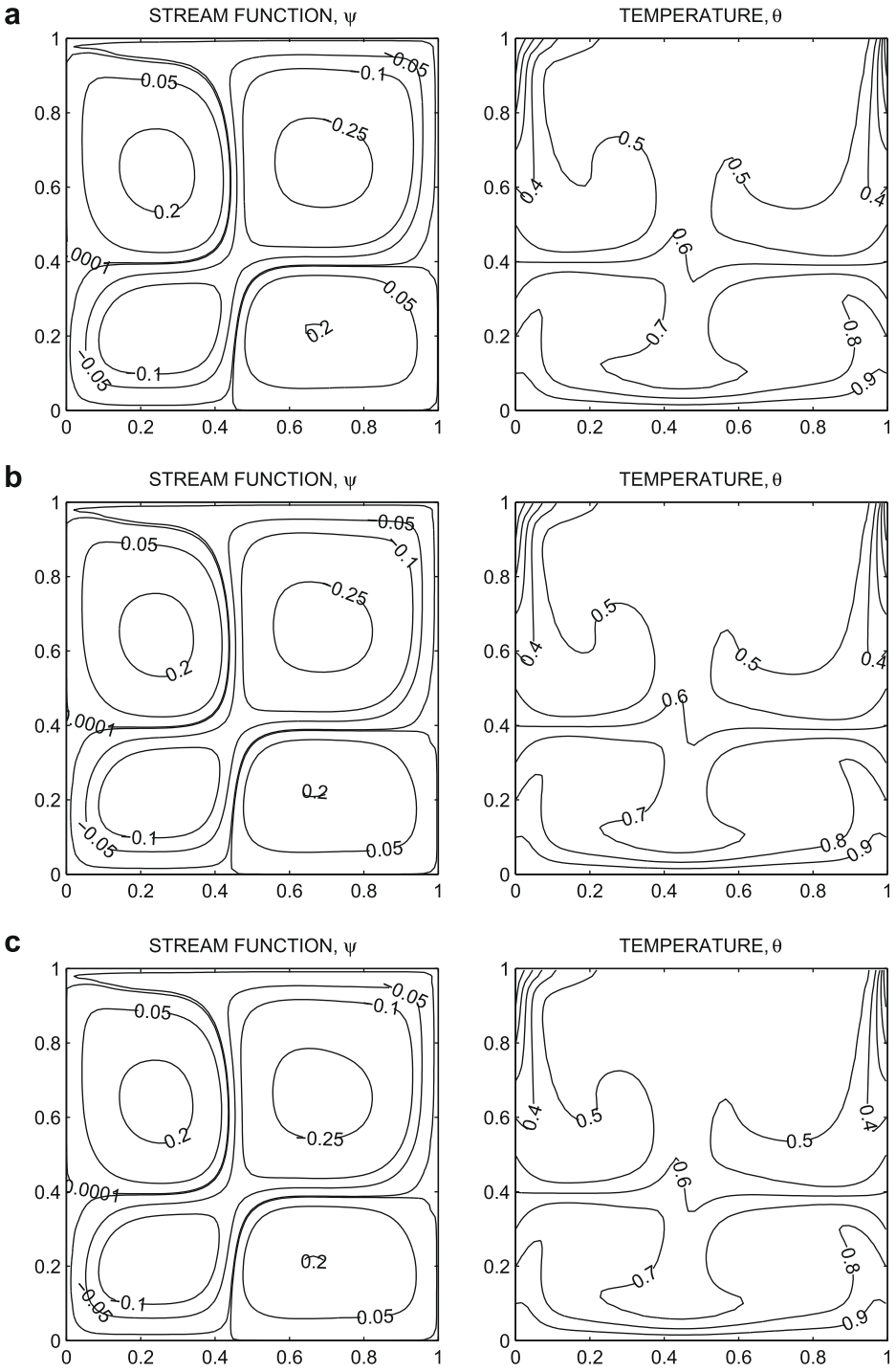


**Fig. 3.** Stream function and temperature contours for linearly heated side walls with $\theta(0,Y)=\theta(1,Y)=1-Y$, $\theta(X,0)=1$, $Pr=10$, $Re=10$ and $Gr=10^5$ for (a) $49\times49$ (b) $57\times57$ and (c) $61\times61$ grid points.

the center of the cavity forming two symmetric rolls with clockwise and anticlockwise rotations inside the cavity (see Fig. 4c). Heat transfer is primarily due to conduction in all these cases ($Gr=10^3-10^5$ and $Pr=0.015$) as the strengths of circulations are lower (see Fig. 4a–c). During conduction dominant heat transfer, the temperature contour for $\theta\leqslant 0.3$ occurs symmetrically near the side of the enclosure. The other temperature contours with $\theta\geqslant 0.4$ are smooth curves which span the entire enclosure and they are generally symmetric with respect to the vertical symmetric line.

Figs. 5 and 6 display results for $Pr=0.7$ and 10, respectively. At $Gr=10^3$, the lid-driven flow is dominant but the isotherms are symmetric representing conduction dominant heat transfer as seen in Fig. 5a. A small amount of secondary circulation with anti-clockwise rotation is found near the top left wall at $Gr=10^4$ (see Fig. 5b). Although the cold fluid is attached with cold upper part of the wall but some part of that fluid is dragged due to the motion of the upper lid. The enhanced convection also leads to the distorted and asymmetric isotherms. The temperature contours for $\theta\leqslant 0.4$ are stretched and are found to be attracted and distorted

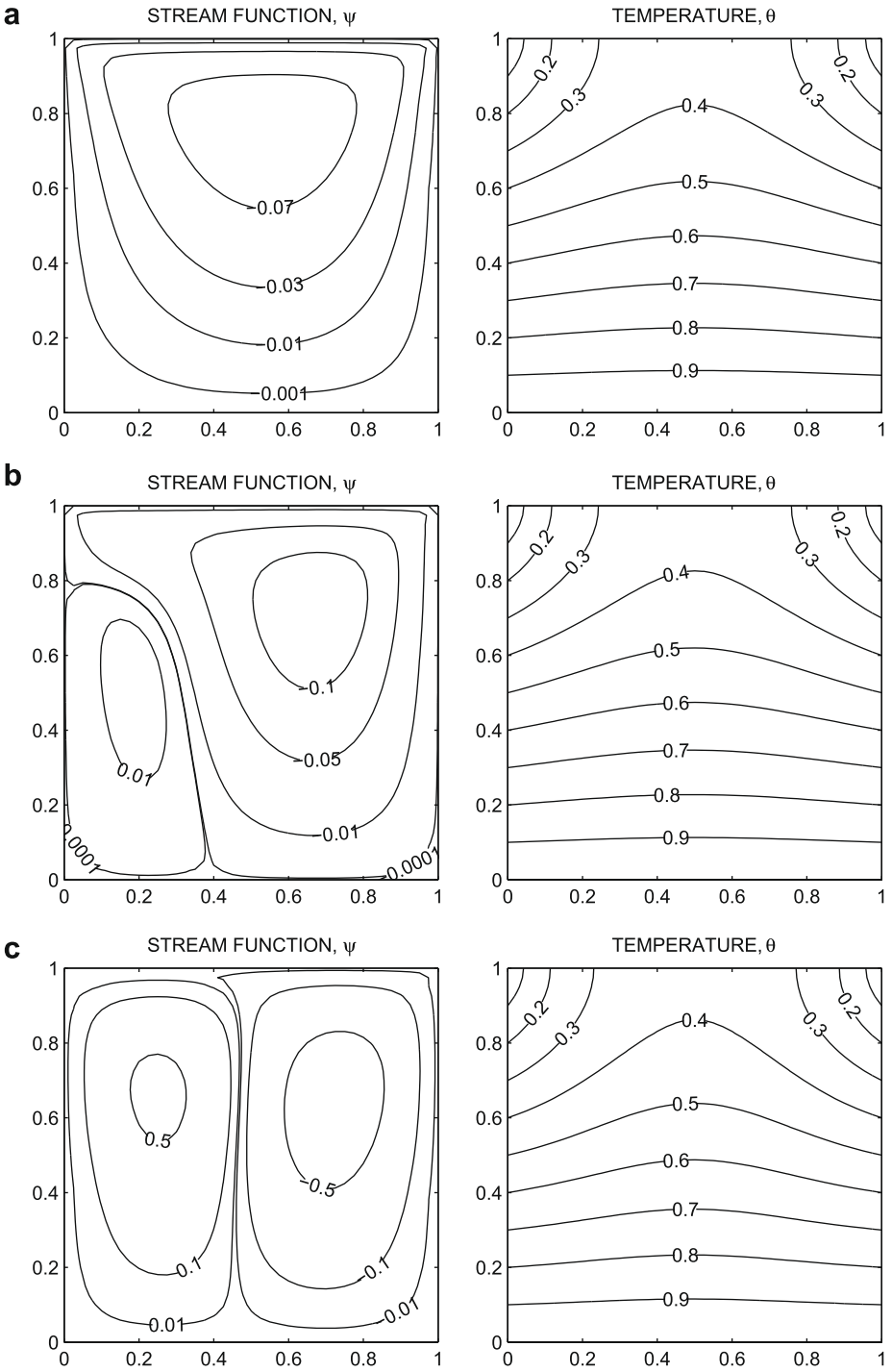


**Fig. 4.** Stream function and temperature contours for linearly heated side walls with $\theta(0,Y)=\theta(1,Y)=1-Y,\ \theta(X,0)=1,\ Pr=0.015,\ Re=10$: (a) $Gr=10^3$ (b) $Gr=10^4$ and (c) $Gr=10^5$.

towards the right corner of the top wall. The other continuous isotherms are also attracted towards the upper wall. As *Gr* increases to $10^5$, two secondary circulations formed inside the cavity as seen in Fig. 5c. Although the fluid in contact with the upper part of the left wall is cold, but a significant amount of the cold fluid is dragged by the motion of the upper lid. Further, another weak secondary circulation appears at the bottom right corner due to strong convection of the warm fluids. It may be noted that the overall intensity of flow at the center of primary and secondary circulation cells is higher and that is due to enhanced effect of natural convection for $Gr=10^5$. It is interesting to observe that a strong primary circulation exists inside the center of the cavity and that increases the mixing process. The isotherms with $\theta \leqslant 0.6$ are disrupted and these isotherms shift towards the cold top portion of side walls due to stronger circulation.

As *Pr* increases to 10, the isotherms are not even symmetric about the central symmetric line for $Gr=10^3$ (see Fig. 6a) and convective heat transfer is found to be dominant. Due to enhanced convection, the upper regime near the right wall experiences thermal mixing and that regime corresponds to $\theta \leqslant 0.4$. At $Gr=10^4$, the primary circulation cell gets deformed towards the middle portion of the right wall and the strength of secondary circulation near

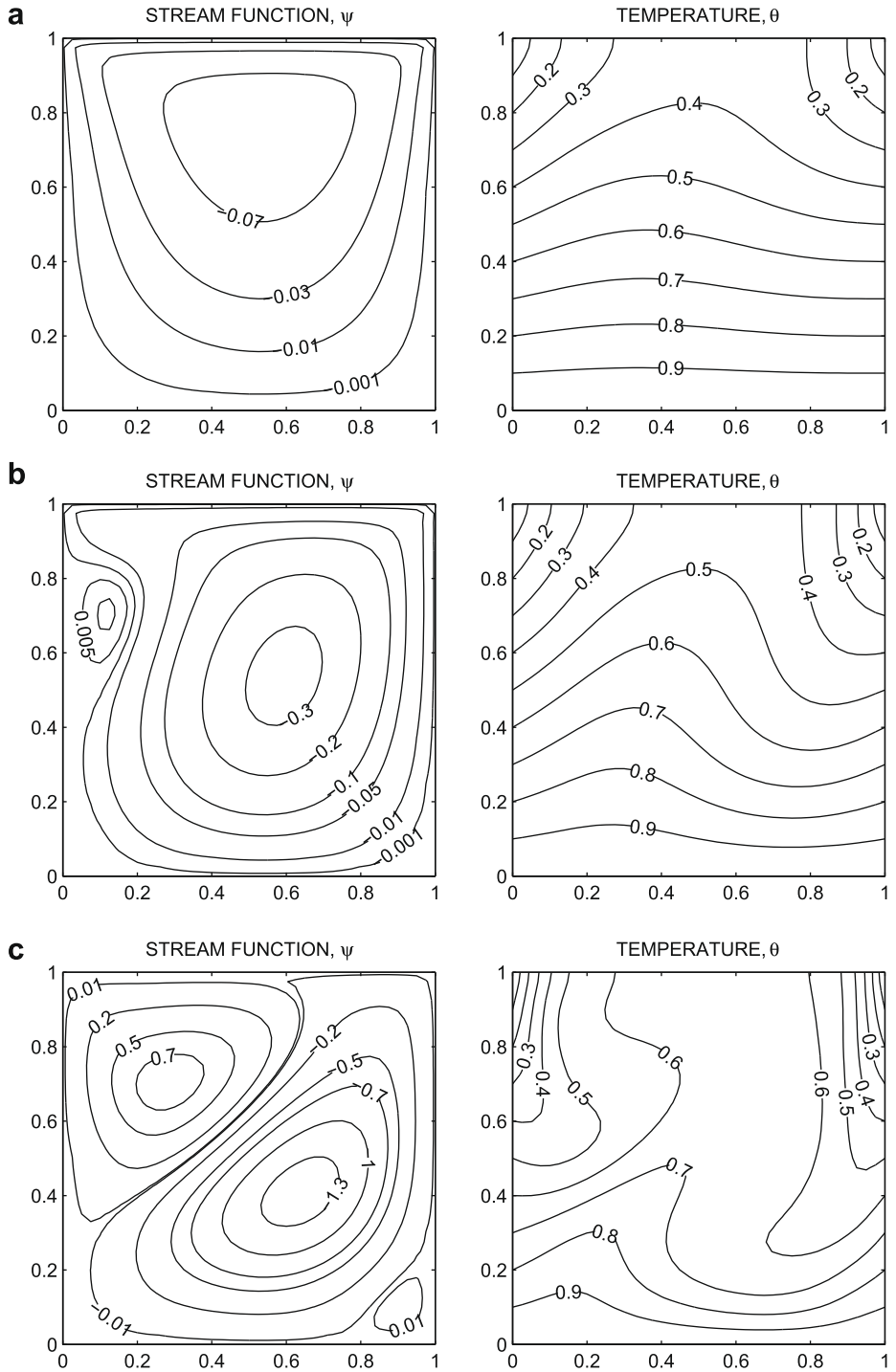


**Fig. 5.** Stream function and temperature contours for linearly heated side walls with $\theta(0,Y)=\theta(1,Y)=1-Y$, $\theta(X,0)=1$, $Pr=0.7$, $Re=10$: (a) $Gr=10^3$ (b) $Gr=10^4$ and (c) $Gr=10^5$.

the bottom portion of the right wall increases as seen in Fig. 6b. The temperature of the major portion of the cavity lies between 0.4 and 0.7 due to enhanced mixing. As *Gr* increases to $10^5$, the secondary circulation cells push the primary circulations towards the upper part of the cavity due to enhanced convection from the hot lower half of the cavity and hot fluid moves towards the center of the cavity as seen from Fig. 6c. It is interesting to observe that the pairs of symmetric circulations with hot and cold fluid regimes appear distinctly inside the cavity and both circulation cells appear due to positive and negative temperature gradients with respect to the center along the vertical walls. The isotherm lines with greater values ($\theta \geqslant 0.5$) cover almost 80% of the cavity.

Fig. 7a–c illustrates the stream function and isotherm contours for $Gr=10^3-10^5, Pr=0.7$ and $Re=10$ with uniformly heated bottom wall, cooled right wall and linearly heated left wall. The effect of lid-driven flow is dominant for low value of *Gr* ($Gr=10^3$) and the fluid rises up along the left hot wall and flows down along the cooled right wall forming a roll with clockwise rotation inside the cavity. As *Gr* increases to $10^5$, the strength of buoyancy inside the cavity increases and more fluid rises from the center

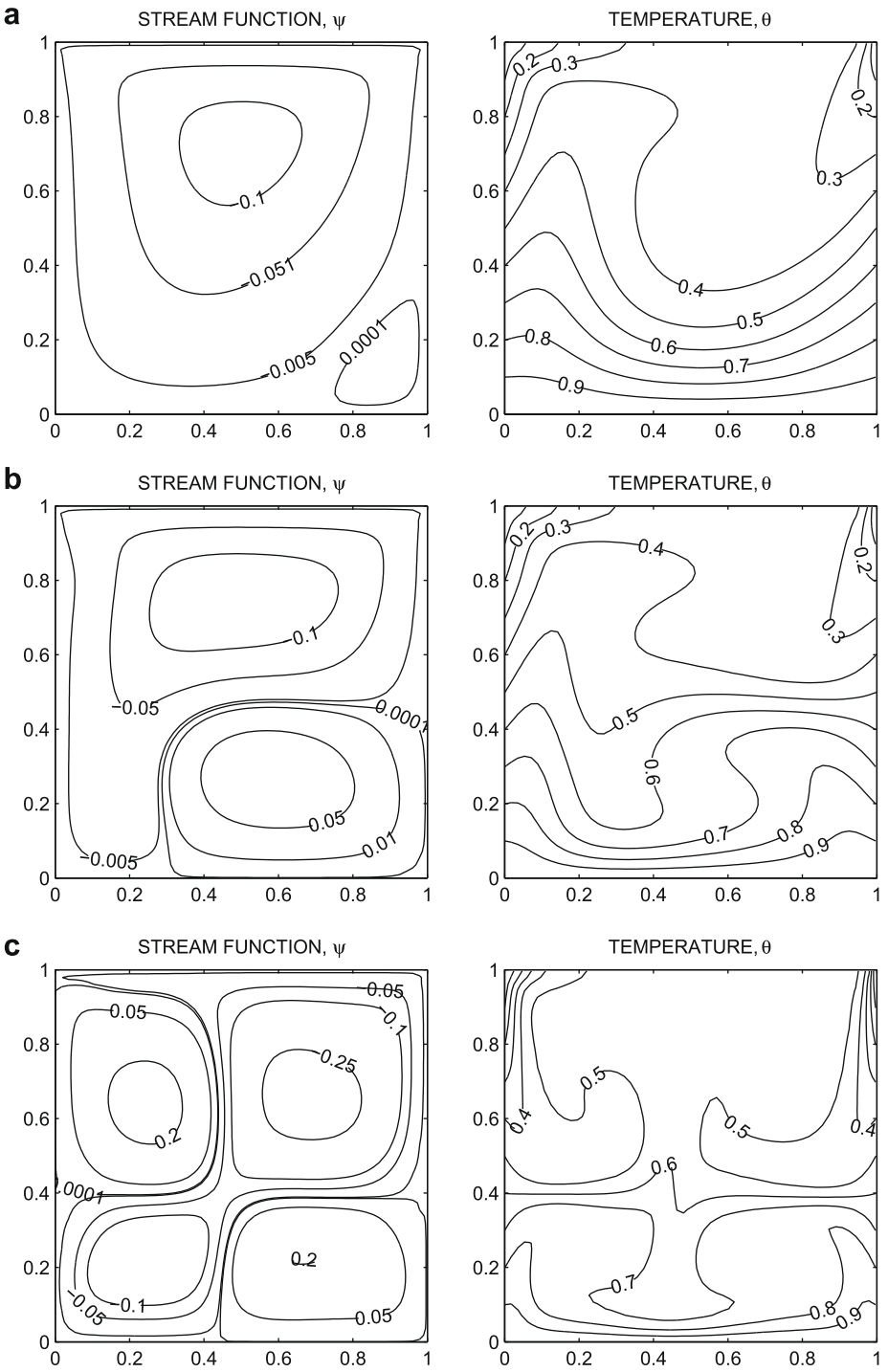


**Fig. 6.** Stream function and temperature contours for linearly heated side walls with $\theta(0,Y) = \theta(1,Y) = 1 - Y$, $\theta(X,0) = 1$, $Pr = 10$, $Re = 10$: (a) $Gr = 10^3$ (b) $Gr = 10^4$ and (c) $Gr = 10^5$.

of the cavity. A secondary circulation is also formed near the top left corner as only a partial amount of fluid is dragged by the motion of the upper lid. The isotherms are found to be non symmetric for all values of *Gr*. The isotherms with $\theta \leqslant 0.2$ are pushed towards the right wall and a small regime of upper portion of left wall whereas the isotherms with $0.3 \leqslant \theta \leqslant 0.7$ are found to vary smoothly from the top portion of the bottom wall for $Gr = 10^3$ (see Fig. 7a). At $Gr = 10^4$, the circulations are stronger and consequently, the temperature contour $\theta \leqslant 0.4$ is pushed towards the cold right wall and a few contours with $\theta = 0.4$–$0.5$ are also pushed towards the top portion of the left wall (see Fig. 7b). As *Gr* increases to $10^5$, the convection inside the cavity increases and the isotherms with $\theta \geqslant 0.5$ occupy nearly 50% of the cavity.

### 4.3. Effect of Reynolds number (Re) for linearly heated side walls or with cooled right wall

Fig. 8a–c shows the effect of *Re* for $Pr = 0.015$ and $Gr = 10^5$. The natural convection is dominant and thus two circulation cells are formed in the cavity at low *Re* ($Re = 1$) as seen in Fig. 8a. The

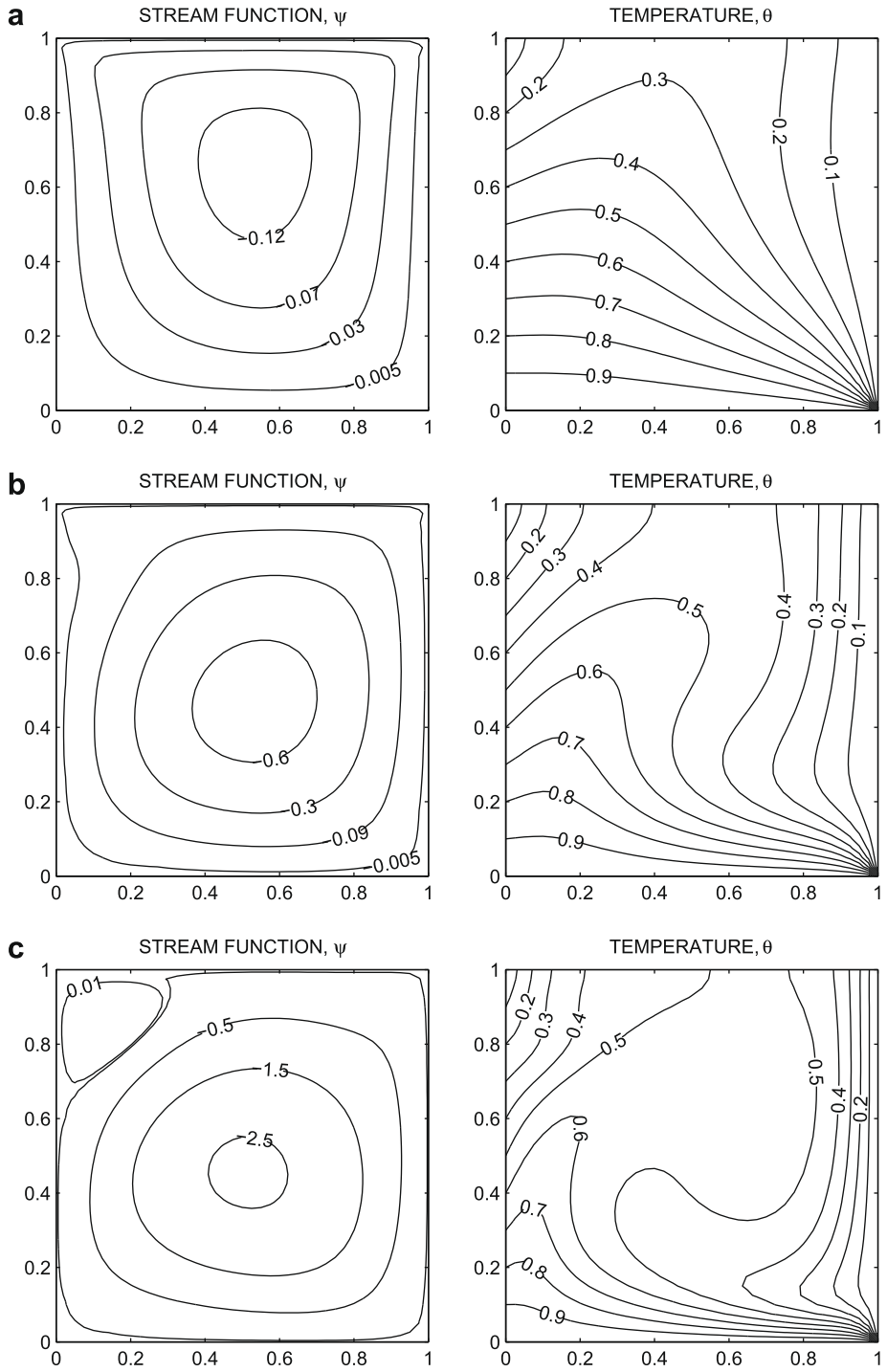


**Fig. 7.** Stream function and temperature contours for linearly heated left vertical wall with $\theta(0,Y) = 1 - Y$ and cooled right vertical wall with $\theta(1,Y) = 0$, $\theta(X,0) = 1$, $Pr = 0.7$, $Re = 10$: (a) $Gr = 10^3$ (b) $Gr = 10^4$ and (c) $Gr = 10^5$.

clockwise and anticlockwise circulation cells are symmetric as the warm fluid rises up from the center and flows symmetrically along the side walls. As *Re* increases to 10, the lid-driven flow gradually start dominating the buoyancy forces. The right vortex is deformed near the top wall due to motion of the upper lid and the left vortex still denotes the dominant effect of natural convection. It may be noted that the buoyancy and inertial forces are in aiding combination near the right wall and only the effects of buoyancy force are present near the left wall. The fluid rises up from the center of the cavity and is pulled towards the right vertical wall due to the motion of the upper lid. Due to this drag force, the primary vortex dominates the secondary vortex and the primary vortex occupies the larger portion of the cavity (see Fig. 8b). As *Re* increases to $10^2$, the secondary circulation almost vanishes inside the cavity and the primary vortex occupies the entire cavity. Thus the effect of buoyancy is suppressed by the enhanced motion of the upper lid as can be seen in Fig. 8c representing the lid-driven flows. Common to all cases, heat is transferred mostly due to conduction and the isotherms with $\theta \leqslant 0.3$ lie symmetrically and isotherms with $\theta = 0.3$–$0.4$ get attracted towards the upper wall for all *Re*

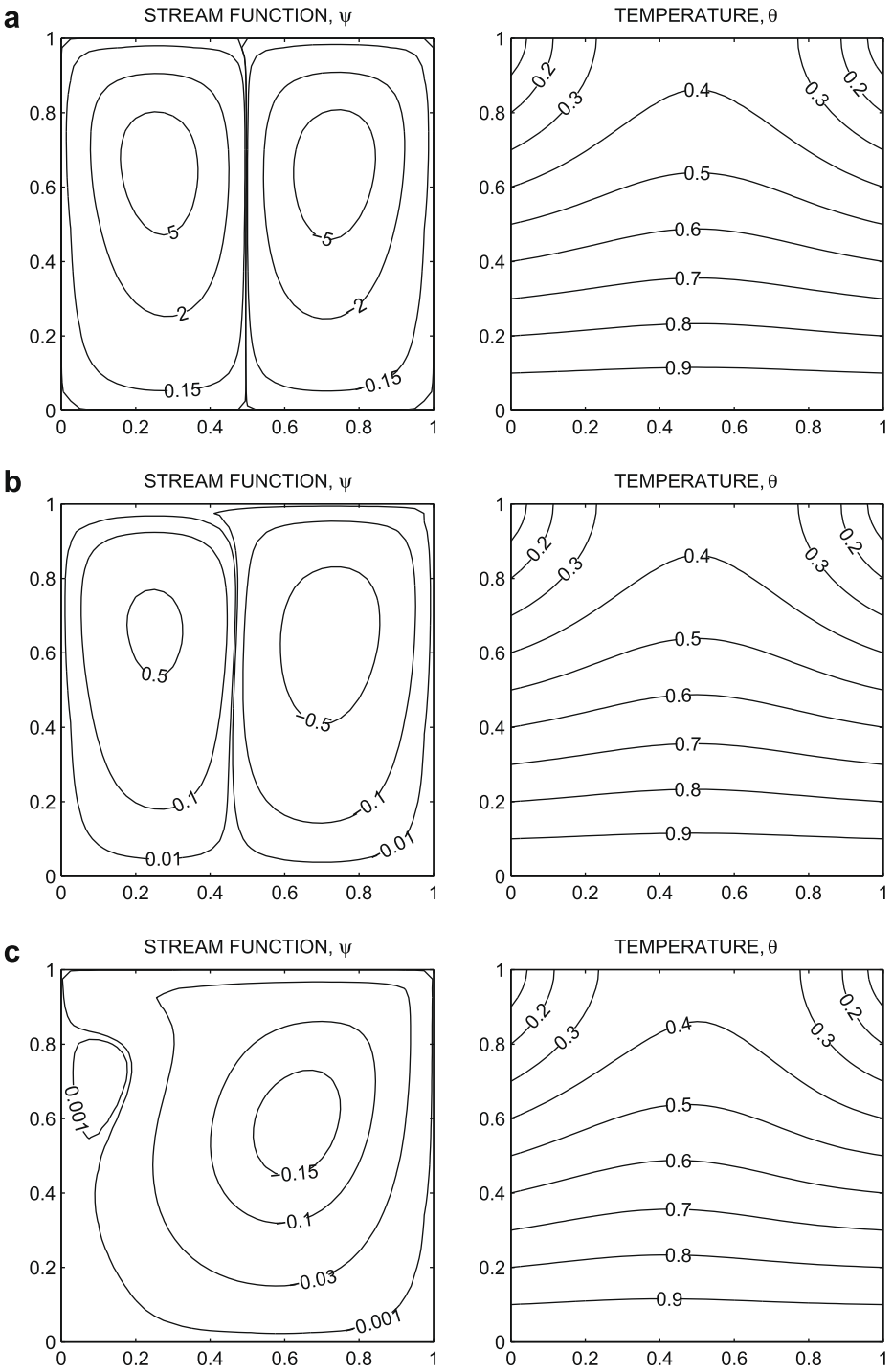


**Fig. 8.** Stream function and temperature contours for linearly heated side walls with $\theta(0,Y)=\theta(1,Y)=1-Y$, $\theta(X,0)=1$, $Pr=0.015$, $Gr=10^5$: (a) $Re=1$ (b) $Re=10$ and (c) $Re=10^2$.

(see Fig. 8a–c). The other isotherms lie symmetrically along the vertical line inside the cavity.

Fig. 9a–c displays the stream function and isotherm contours for $Pr=0.7, Gr=10^5$ and with various values of $Re$. It is interesting to observe that a strong secondary vortex is formed at the top left corner and another weaker secondary vortex is also formed at the bottom right corner for $Re=1$ as seen in Fig. 9a. The vortex at the top left corner is formed due to the fact that the cold fluid is partly dragged by the motion of the upper lid. Further the vortex at the bottom left corner is formed due to convection of the warm fluid. It is also interesting to note that the maximum value of the stream function in the primary cell is 12 and that implies intense convection (natural convection as well as forced convection). Therefore, the significant effect of mixed convection is observed for $Re=1$ and $Pr=0.7$ and that contrasts the effect of dominant natural convection at $Pr=0.015$ and $Re$ as seen in Fig. 8a. Due to significant effect of mixed convection and enhanced thermal mixing, the temperature of the major portion of the cavity lies between 0.5 and 0.7 and these isotherms occupy nearly 80% of the cavity (see Fig. 9a). It is interesting to observe that the isotherms are highly compressed

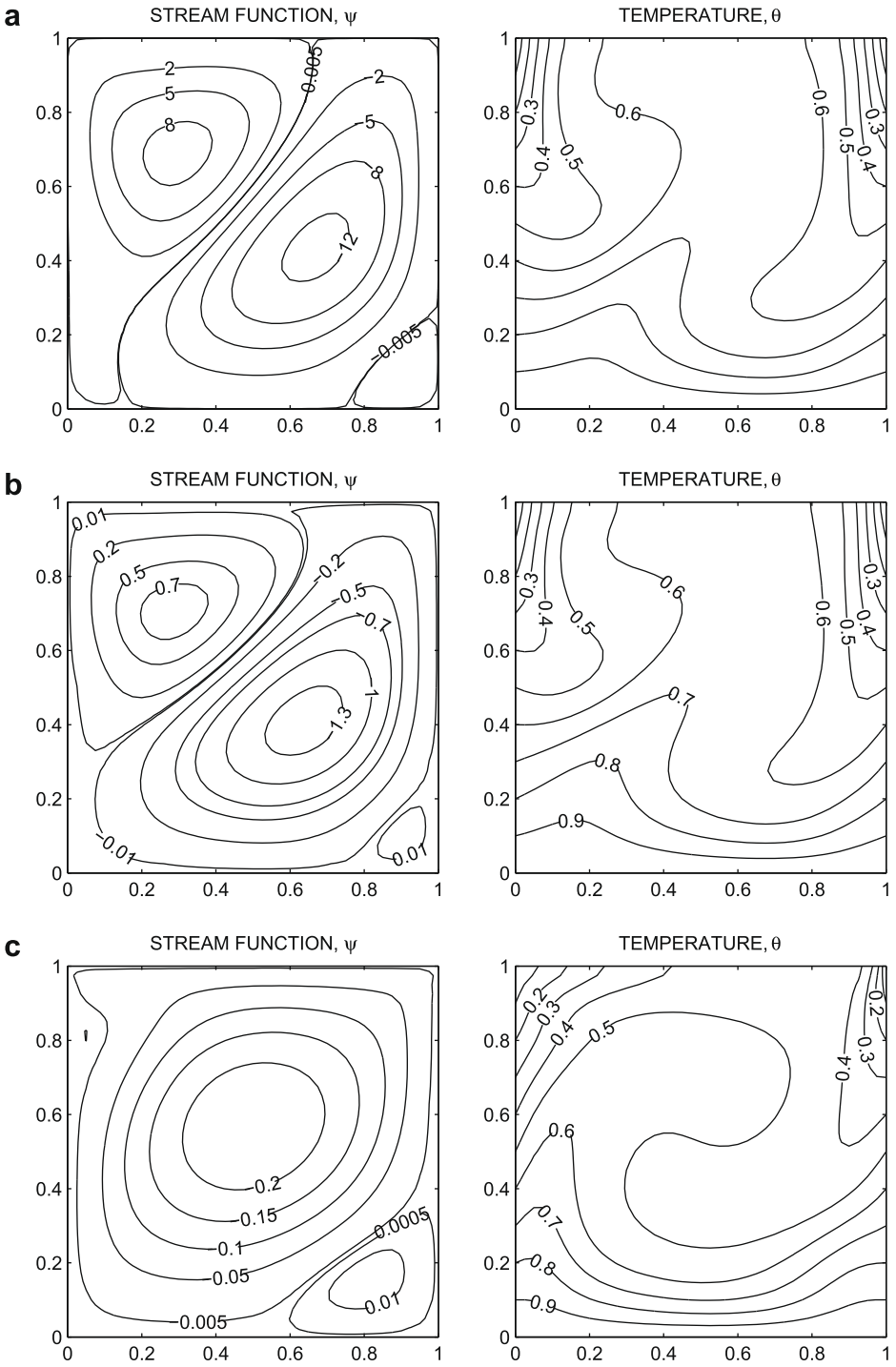


**Fig. 9.** Stream function and temperature contours for linearly heated side walls with $\theta(0,Y)=\theta(1,Y)=1-Y$, $\theta(X,0)=1$, $Pr=0.7$, $Gr=10^5$: (a) $Re=1$ (b) $Re=10$ and (c) $Re=10^2$.

near the top portion of side walls due to strong convective effects. Similar patterns are also observed for stream function and isotherms at $Re=10$ (see Fig. 9b). It may be noted that, the strength of circulation decreases as seen in Fig. 9b and the strength of circulation is lesser from that of Fig. 9a. As $Re$ increases to $10^2$, the secondary vortex at the top left corner disappears due to enhanced motion of the upper lid that drags more fluid from left to right part of the cavity (Fig. 9c). But the other secondary vortex remains at the bottom right corner due to presence of two distinct layers of fluid near the right wall. The cold fluid is dragged by the motion of the upper lid leaving the warm fluid near the bottom right corner. The isotherms with $\theta \leqslant 0.4$ are compressed and attracted towards the top wall especially near the top portion of the right wall due to strong primary circulation cell.

Fig. 10 displays the effect of $Re$ for $Pr=0.7$ and $Gr=10^5$ with cooled right wall. At $Re=1$, the major part of the cavity is occupied by primary vortex and a small part near the top left corner is occupied by the secondary vortex (see Fig. 10a). This is due to fact that only a partial amount of fluid is dragged by the motion of the upper lid. The isotherms for $\theta \leqslant 0.4$ get highly compressed towards the

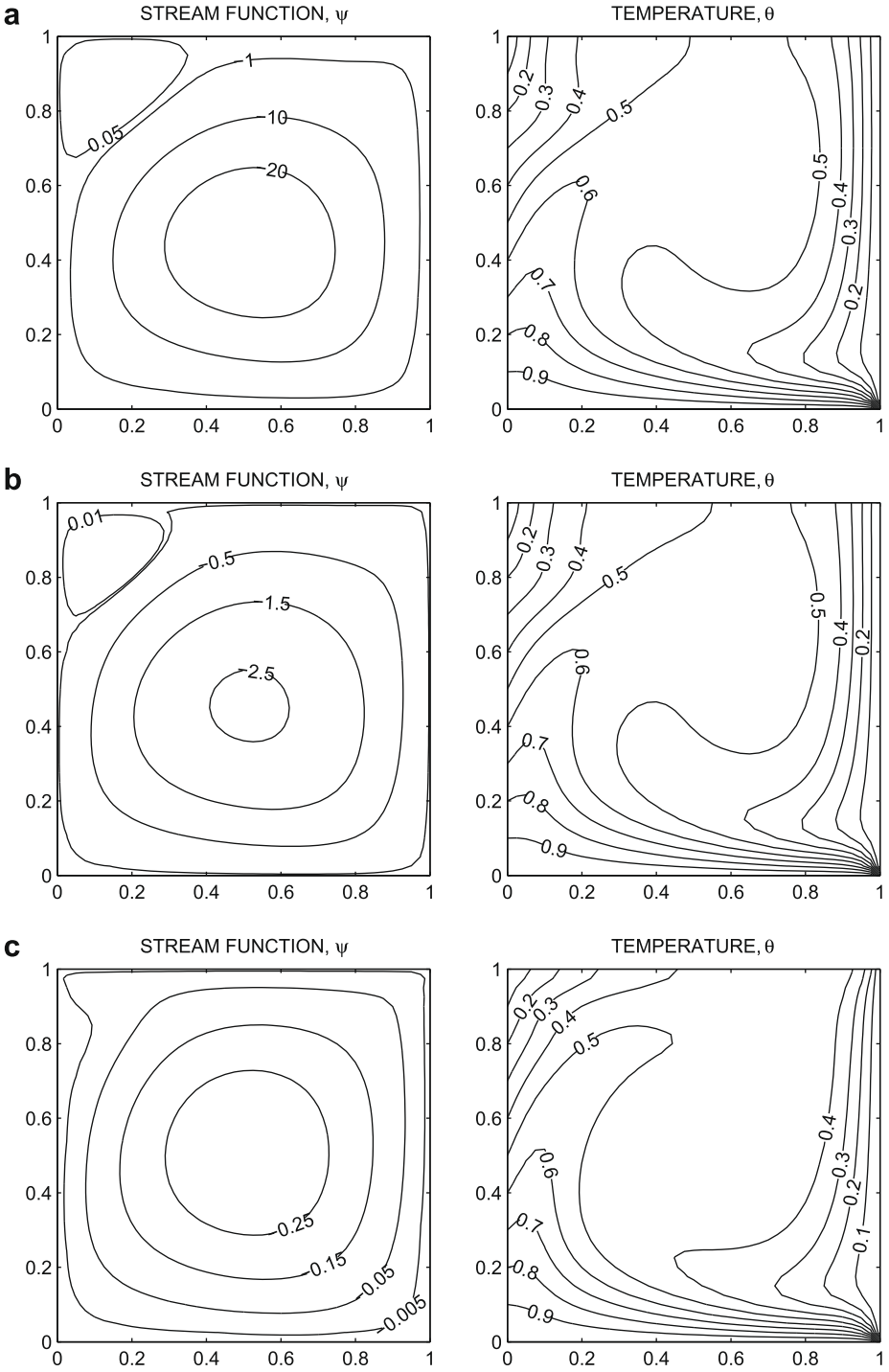


**Fig. 10.** Stream function and temperature contours for linearly heated side wall with $\theta(0,Y) = 1 - Y$, cooled right wall with $\theta(1,Y) = 0,\ \theta(X,0) = 1,\ Pr = 0.7,\ Gr = 10^5$: (a) $Re = 1$ (b) $Re = 10$ and (c) $Re = 10^2$.

cold portion of side wall and the temperature of the major part of the cavity is maintained at $\theta = 0.5$. As *Re* increases to 10, a similar qualitative pattern of streamlines and isotherms appear as seen in Fig. 10a and b. As *Re* increases to $10^2$, the secondary circulation disappears and the whole cavity is occupied by primary vortex only (see Fig. 10c). The streamlines appear to be almost circular. This represents the case of lid-driven flow. The temperature of the major part of the cavity lies in between 0.4 and 0.5.

As *Pr* increases to 10, the secondary circulation becomes more prominent for $Re = 1$ and 10. The isotherms are highly compressed towards the right portion of the bottom wall and cooled right wall. The temperature of the major part of the cavity lies in between 0.4 and 0.5 and a small portion at the center corresponds to $\theta = 0.5$ (see Fig. 11a and b). As *Re* increases to $10^2$, the streamlines near the boundary appear to be rectangular and at the center it appears to be oval. The rectangular streamlines near the walls denote enhanced mixing. It may be noted that the secondary vortex completely disappears and uniform thermal mixing is observed as $\theta = 0.3$–$0.4$ is maintained in 90% of the cavity (see Fig. 11c).

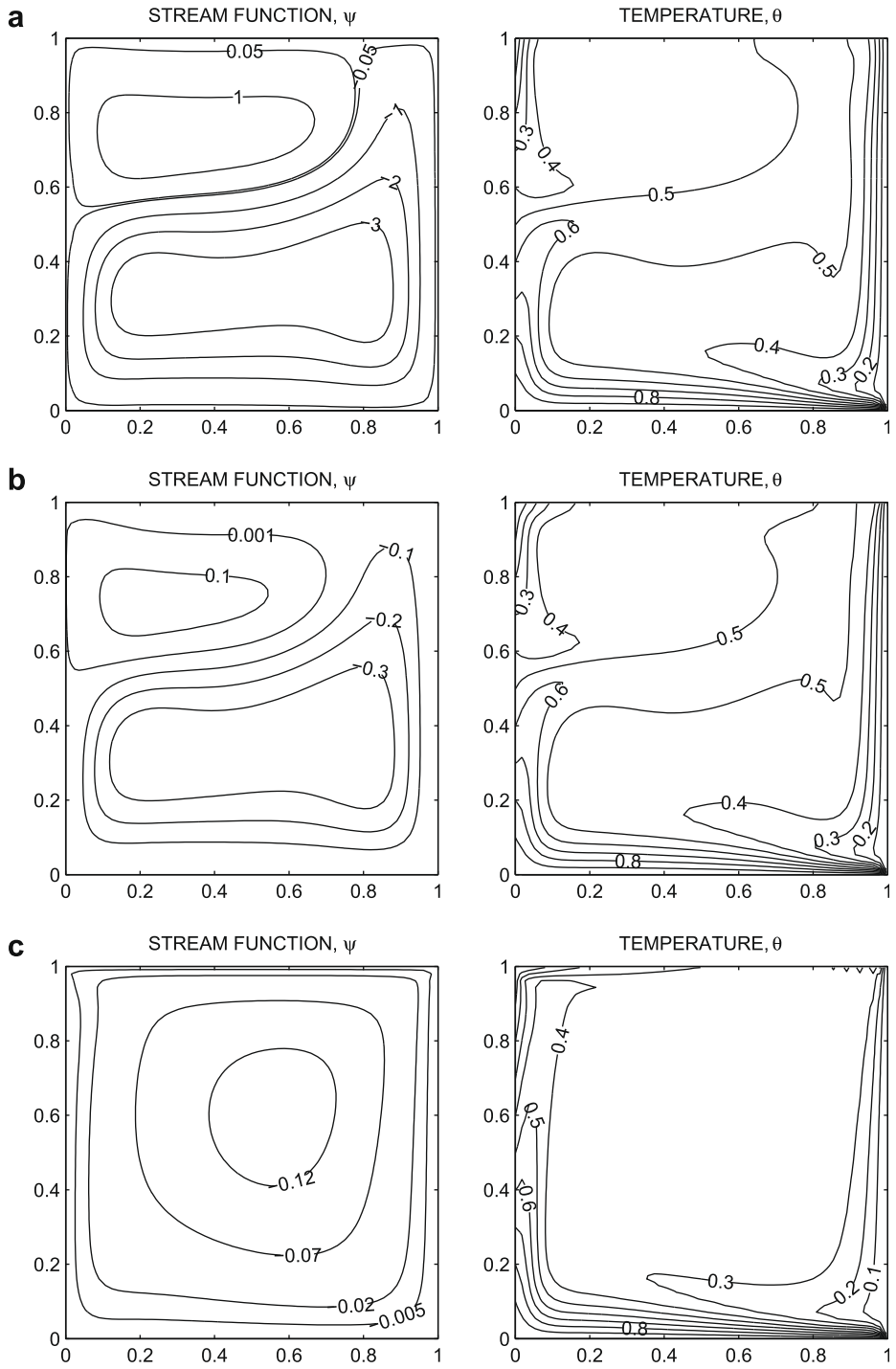


**Fig. 11.** Stream function and temperature contours for linearly heated side wall with $\theta(0,Y) = 1 - Y$, cooled right wall with $\theta(1,Y) = 0,\ \theta(X,0) = 1,\ Pr = 10,\ Gr = 10^5$: (a) $Re = 1$ (b) $Re = 10$ and (c) $Re = 10^2$.

*4.4. Heat transfer rate: Local and average Nusselt numbers for linearly heated side walls or cooled right wall*

Fig. 12a shows the effect of local heat transfer rate along the bottom wall for various values of *Pr* with $Gr = 10^3$ and $10^5$ and $Re = 10$ in presence of linearly heated side walls. At the edges of the bottom wall the heat transfer rate ($Nu_b$) is 1 due to linearly heated side walls. The heat transfer rate is uniformly equal to 1 throughout the wall at $Pr = 0.015$ due to isotherms being parallel to the bottom wall based on the dominance of conduction. As *Pr* increases to 0.7, the heat transfer rate ($Nu_b$) is larger due to enhanced intensity of circulations for $0.3 \leqslant X \leqslant 0.9$ (Fig. 5a). In addition, $Nu_b$ attains the maxima in the right part of the cavity due to compression of isotherms along the right wall. The compression of isotherms is further increased due to enhanced circulations with the increase of *Pr* ($Pr = 10$) as seen in Fig. 6a. The compression of isotherms is pronounced within $0.4 \leqslant X \leqslant 0.6$ and $Nu_b$ is large within that regime. It is interesting to note that $Nu_b$ vs distance with $Gr = 10^3$ and $10^5$ are identical for $Pr = 0.015$. As *Gr* increases to $10^5$, heat transfer rate along the bottom wall ($Nu_b$) for $Pr = 0.7$ and 10 is larger than that with $Gr = 10^3$. It may be noted that $Nu_b$ is largest at $X = 0.7$ and 0.4 for $Pr = 0.7$ and 10, respectively

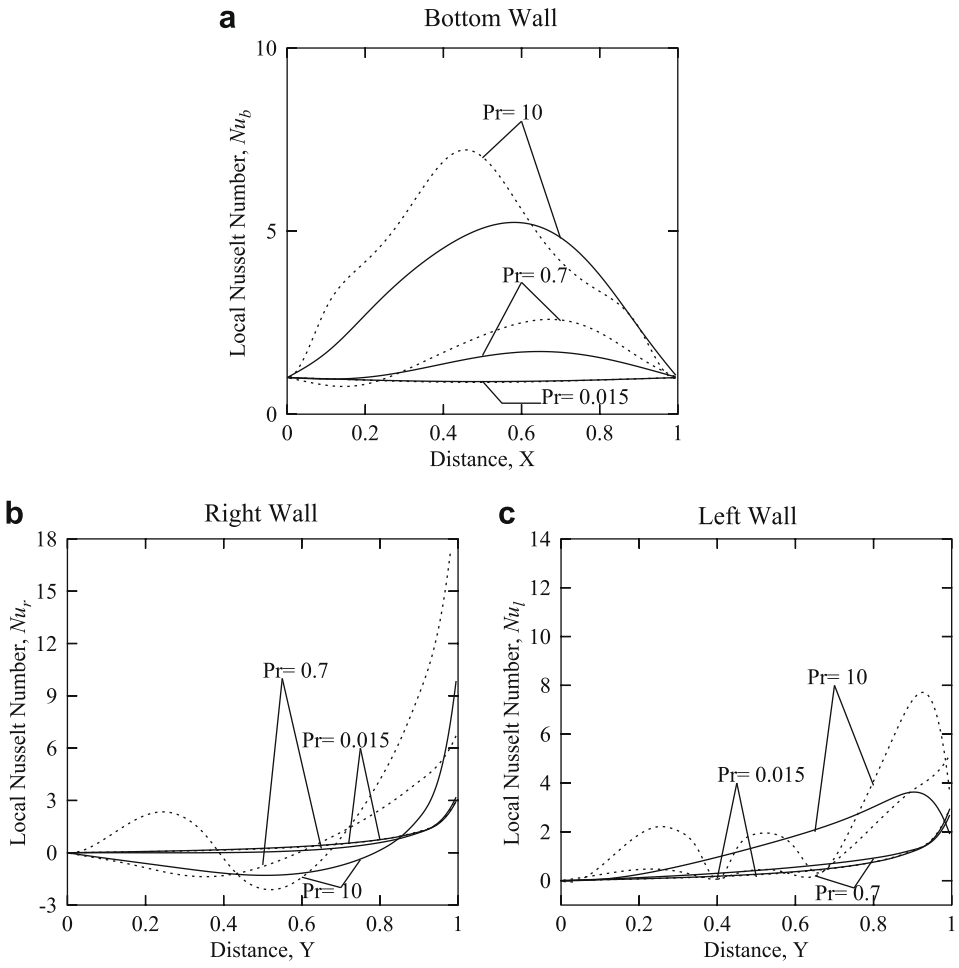


**Fig. 12.** Variation of Local Nusselt number with distance at the (a) bottom wall (b) right wall and (c) left wall for linearly heated side walls with $Re = 10$, $Gr = 10^3$ (—) and $10^5$ (...).

due to highly compressed isotherms resulting from enhanced convection at $Gr = 10^5$.

Fig. 12b shows the effect of local heat transfer rate along the right wall ($Nu_r$) for various values of $Pr$ with $Gr = 10^3$ and $10^5$. The heat transfer rate at the bottom edge of the side walls is zero due to uniformly heated bottom wall and widely dispersed isotherms. It is interesting to observe that $Nu_r$ has a maxima at the top edge due to large temperature gradient for all values of $Pr$ and $Gr$. It may be noted that the heat transfer rate, $Nu_r$ is almost zero for $Gr = 10^3$, $Pr = 0.015$ and $Pr = 0.7$ upto $Y = 0.7$ due to widely dispersed isotherms and $Nu_r$ is 3 at $Y = 1$ due to dense isotherms contours (Fig. 12b). It is also interesting to observe that the heat transfer rate ($Nu_r$) is negative upto $Y = 0.8$ for $Pr = 10$ due to widely dispersed isotherms as seen in Fig. 6a. The thermal gradient is least at around $Y = 0.7$ and afterwards, $Nu_r$ is increased upto 9 at the top edge due to large thermal gradient as seen in Fig. 6a. It is also interesting to observe that $Nu_r$ vs distance remains invariant of $Gr$ for $Pr = 0.015$. Similar characteristics are also found for $Nu_b$ or $Nu_l$ vs distance profile. As $Gr$ increases to $10^5$, $Nu_r$ decreases upto $Y = 0.3$ for $Pr = 0.7$ and then that increases with the increase of vertical distance. The initial decrease in $Nu_r$ with the distance is due to widely dispersed isotherms as seen in Fig. 5c. The hot fluid near the bottom portion of the right wall is taken away by primary circulation and that reduces the thermal gradient near the bottom portion of the right wall. As $Pr$ increases to 10, $Nu_r$ shows oscillatory behavior with the maxima and minima attaining in alternate manner. This is due to the compression of isotherms towards the bottom wall and the top portion of the right wall due to recurrence of pair of circulations as seen in Fig. 6c.

Fig. 12c illustrates that $Nu_l$ is almost zero upto $Y = 0.7$ and thereafter $Nu_l$ increases for $Pr = 0.015$ and 0.7 with $Gr = 10^3$. Similar characteristics were also observed for the right wall. On the other hand, for $Pr = 10$ and $Gr = 10^3$, $Nu_l$ increases upto $Y = 0.9$ and thereafter that decreases. The sudden decrease in $Nu_l$ is due to the fact that the cold fluid at the top portion of the left wall is dragged by the top moving wall and therefore the top portion of the left wall remains cold and the temperature gradient is less as $\theta$ is varying within 0.1–0.2 (see Fig. 6a). As $Gr$ increases to $10^5$, $Nu_l$ shows more number of oscillations with $Y$ especially at $Pr = 10$ due to compression of isotherms at various locations resulting from dominant effect of convection. Similar phenomena was also observed for right wall. However, frequency of oscillation is larger for $Nu_l$ due to drag of liquid along the right direction of the top wall.

Fig. 13a–c displays the heat transfer rate along the bottom, right and left walls, respectively with linearly heated left wall and cooled right wall. Fig. 13a shows that $Nu_b$ increases from the left edge towards the right edge of the bottom wall. The heat transfer rate ($Nu_b$) is 0 at the left edge of the bottom wall due to linearly heated left wall and that is maximum at the right edge due to cooled right wall attached with the hot bottom wall. It is interesting to note that $Nu_b$ is larger along the bottom wall for $Pr = 10$ due to enhanced compression of isotherms. The qualitative trends in $Nu_b$ are similar for $Gr = 10^3$ and $10^5$. Although distribution of $Nu_b$ is found to be invariant of $Gr$ for $Pr = 0.015$, but larger

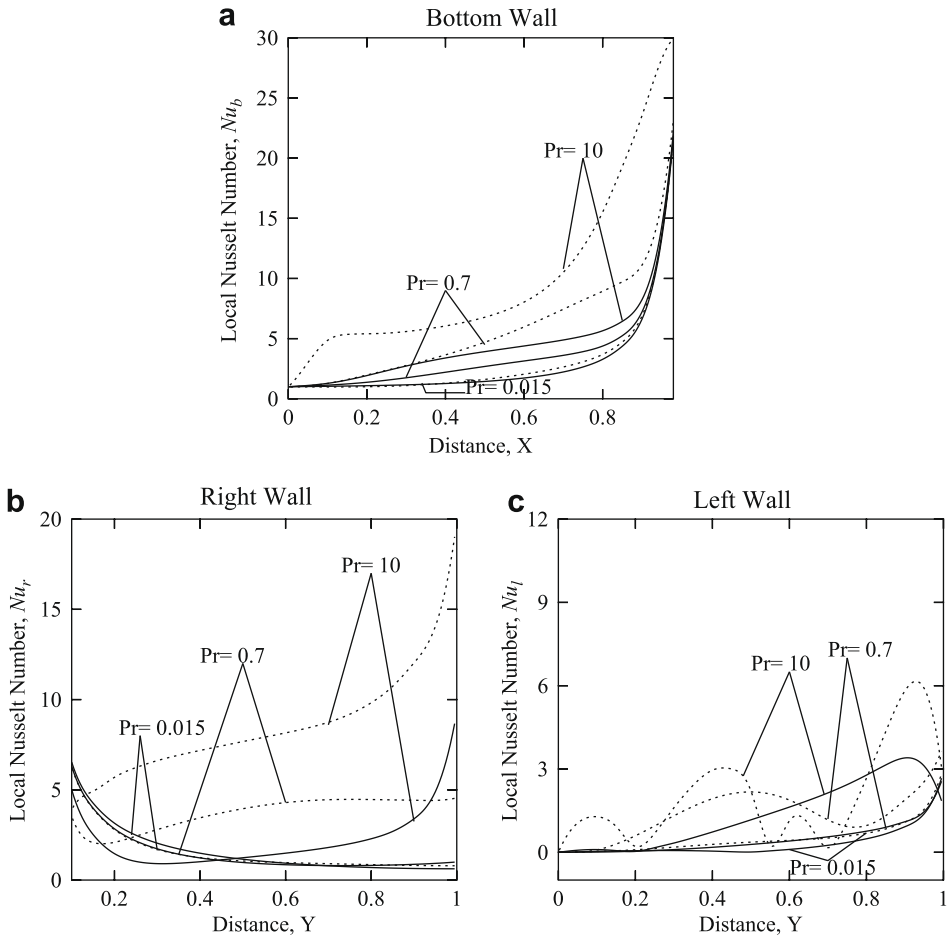


**Fig. 13.** Variation of Local Nusselt number with distance at the (a) bottom wall (b) right wall and (c) left wall for linearly heated left wall and cooled right wall with $Re = 10$, $Gr = 10^3$ (—) and $10^5$ (...).

compression of isotherms occur for $Pr = 0.7$ and 10 leading to high value of $Nu_b$ at $Gr = 10^5$.

Fig. 13b illustrates that $Nu_r$ decreases for $Pr = 0.015$ and 0.7 with $Gr = 10^3$. This is due to the fact that for lower value of $Pr$, the effect of conduction is dominant and the isotherms are attracted towards the bottom edge of the right wall due to singularity present at the corner of the right wall. As $Pr$ increases to 10, $Nu_r$ first decreases upto $Y = 0.2$ and thereafter that increases with the increase of vertical distance as the isotherms are distorted due to dominant effect of convection and are attracted towards the top portion of the right wall. It is important to note that, the boundary layer starts to grow at the bottom edge of the right wall and the thickness is larger at $Y = 0.2$. Thereafter, the thickness of boundary layer is smaller leading to large value of $Nu_r$. At $Gr = 10^5$, the thickness of boundary layer is larger near the bottom edge of the right wall and the isotherms are found to be highly compressed along the top portion of the wall due to enhanced circulation especially for $Pr = 0.7$ and 10.

Fig. 13c shows that the heat transfer rate ($Nu_l$) at the bottom edge of the left wall is zero due to linearly heated left wall and its magnitude increases from the bottom to top edge of the left wall especially for $Pr = 0.7$ and 10. The heat transfer rate ($Nu_l$) is found to be increasing for $Y \geqslant 0.2$ and afterwords that decreases for $Y \geqslant 0.9$ for $Pr = 10$ at $Re = 10$. Similar phenomena is also observed for linearly heated side walls as seen in Fig. 12c. As $Gr$ increases to $10^5$, $Nu_l$ shows oscillatory behavior due to presence of secondary circulation near the top edge of the left wall. In addition, the isotherms are quite disperse at the bottom portion of the left wall. Similar to Fig. 12c, $Nu_l$ is greater with $Gr = 10^5$ than that with $Gr = 10^3$ at the top edge for $Pr = 10$. This is due to the fact that the isotherms at the top edge of the left wall are distorted and compressed for $Gr = 10^5$ as seen in Fig. 11b.

The overall effects on heat transfer rates are shown in Fig. 14(a–d), where the distributions of the average Nusselt number at bottom and side walls, respectively, are plotted as functions of logarithmic Grashof number or Richardson number. The average Nusselt numbers are obtained using Eqs. 18 and 19 where the integral is evaluated using Simpson's 1/3 rule. Fig. 14a and b displays $\overline{Nu_b}$ and $\overline{Nu_l}$, respectively, for the case of linearly heated side walls while Fig. 14c and d represents average Nusselt number for the case of linearly heated left wall and cooled right wall with $Pr = 0.015$, 0.7 and 10. The inset plot of Figs. 14b and d illustrates the average Nusselt number distributions for right wall. The average heat transfer rate for $Pr = 0.015$ is constant in all cases due to dominant effect of conduction (Fig. 14a–d).

Fig. 14a shows that $\overline{Nu_b}$ is constant upto $Gr = 8 \times 10^3$ and thereafter that increases for $Pr = 0.7$. This is due to the fact that the isotherms are compressed with the increase of $Gr$ leading to larger $Nu_b$ near the middle portion of the bottom wall (Fig. 12a) and as a result heat transfer rate increases along the bottom wall. It is also observed that $\overline{Nu_b}$ increases for $Pr = 10$ due to compression of isotherms resulting from enhanced convection. The enhancement of $\overline{Nu_b}$ with $Gr$ is also due to larger $Nu_b$ for higher $Gr$.

Fig. 14b illustrates that $\overline{Nu_l}$ with $Pr = 10$ shows oscillation with the increase of $Gr$. The oscillations of $\overline{Nu_l}$ at higher $Gr$ is also attributed to the larger degree of oscillation of $Nu_l$ with distance at

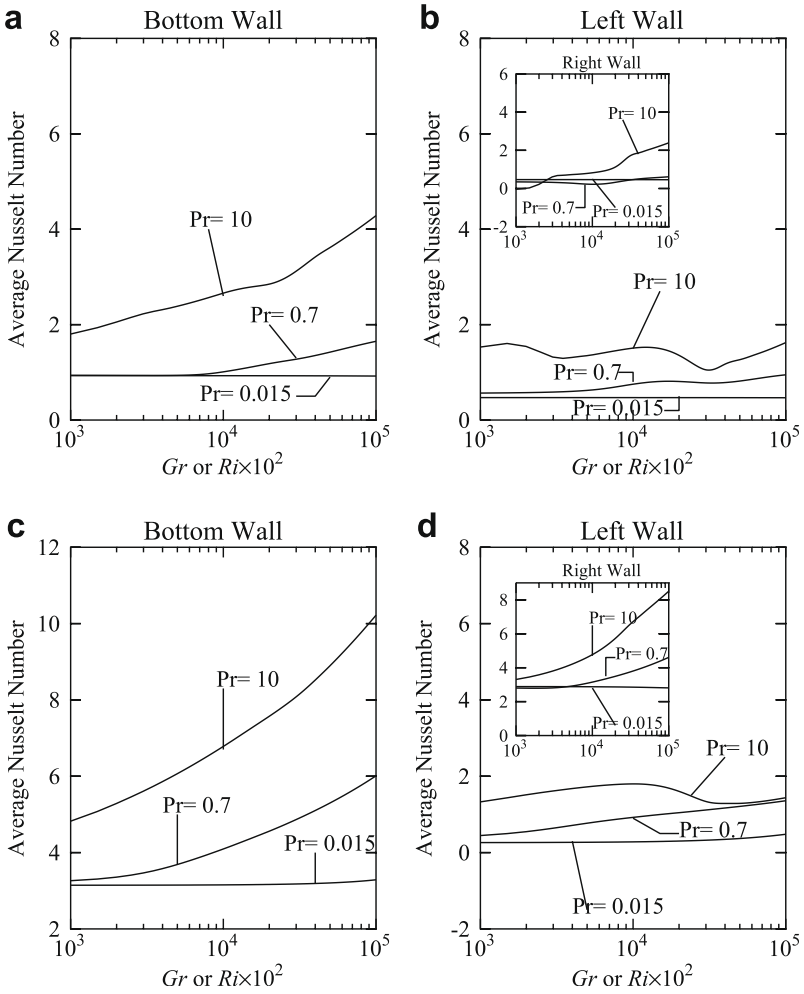


**Fig. 14.** Variation of average Nusselt number with $Gr$ or $Ri \times 10^2$ for linearly heated side walls (a and b) and linearly heated left wall and cooled right wall (c and d) with $Pr = 0.015; Pe = 0.15$, $Pr = 0.7; Pe = 7$, $Pr = 10; Pe = 10^2$.

$Gr = 10^5$ as seen in Fig. 12c. The inset plot shows that $\overline{Nu_r}$ for $Pr = 0.7$ decreases upto $Gr = 10^4$ and thereafter that increases. This is due to the fact that isotherms are widely dispersed upto $Gr = 10^4$ as seen in Fig. 5a–b. Similar to the left wall, $\overline{Nu_r}$ also shows oscillation for $Pr = 10$ as $Nu_r$ shows oscillations with distance at $Gr = 10^5$ as seen in Fig. 12b.

Fig. 14c shows that $\overline{Nu_b}$ for $Pr = 0.7$ and 10 increases smoothly with the increase of $Gr$. Fig. 14d shows that $\overline{Nu_l}$ vs $Gr$ for $Pr = 0.015$ and 0.7 is qualitatively similar as seen in Fig. 14b. As $Pr$ increases to 10, $\overline{Nu_l}$ increases upto $Gr = 3 \times 10^4$ and then that decreases sharply. This is due to the presence of oscillations in $Nu_l$ vs distance as seen in Fig. 13c and sharp decrease may occur due to localized dispersed isotherms at higher $Gr$. The inset shows that $\overline{Nu_r}$ for $Pr = 0.7$, is constant upto $Gr = 8 \times 10^3$ and thereafter that increases. This is due to the fact heat transfer is dominated by conduction upto $Gr = 10^4$ and thereafter by convection. On the other hand, $\overline{Nu_r}$ for $Pr = 10$ increases smoothly with the increase of $Gr$.

Variation of average Nusselt number vs Prandtl number or Peclet number with various Grashof numbers are shown in Fig. 15a–d. Fig. 15a and b illustrates variations for the case corresponding to linearly heated side walls and Fig. 15c and d shows variations for linearly heated left wall in presence of cold vertical wall. It is observed that variation of average Nusselt number with Grashof number is not significant for $Pr \leqslant 0.5$ for all cases. In general, average Nusselt numbers increase with $Pr$ for specific Grashof numbers. It is also found that $\overline{Nu_b}$ is large for $Pr \geqslant 5$ and $Gr = 10^5$. Average Nusselt numbers for the bottom wall ($\overline{Nu_b}$) for the case with cold right wall are larger than those for the case with linear heated side walls (see Fig. 15a and c). It is interesting to observe that $\overline{Nu_l}$ is found to be weaker functions of Grashof numbers for all ranges of $Pr$ (see Fig. 15b and d) whereas average Nusselt numbers for the right wall ($\overline{Nu_r}$) are larger for $Gr = 10^5$ at larger values of $Pr$ for all the cases (see insets of Fig. 15b and d).

## 5. Conclusions

The influence of linearly heated vertical walls or cooled right wall with uniformly heated bottom wall on flow and heat transfer characteristics due to mixed convection within a square cavity has been studied in the present investigation. The penalty finite element method helps to obtain smooth solution in terms of stream function and isotherm contours. It is observed that the effect of lid-driven flow is dominant for $Gr = 10^3$ and as the value of $Gr$ increases both the primary and secondary circulations appear inside the cavity. This is due to the increase of buoyancy force with the increase of $Gr$. Heat transfer is primarily due to conduction for all values $Gr$ with $Pr = 0.015$. There occurs a transition from conduction to convection at $Gr = 8 \times 10^3$ for $Pr = 0.7$. For higher value of $Pr$ ($Pr = 10$), the isotherms are not symmetric about the central line for smaller $Gr$ ($Gr = 10^3$) and convective heat transfer is found to be dominant for linearly heated side walls. It is interesting to note

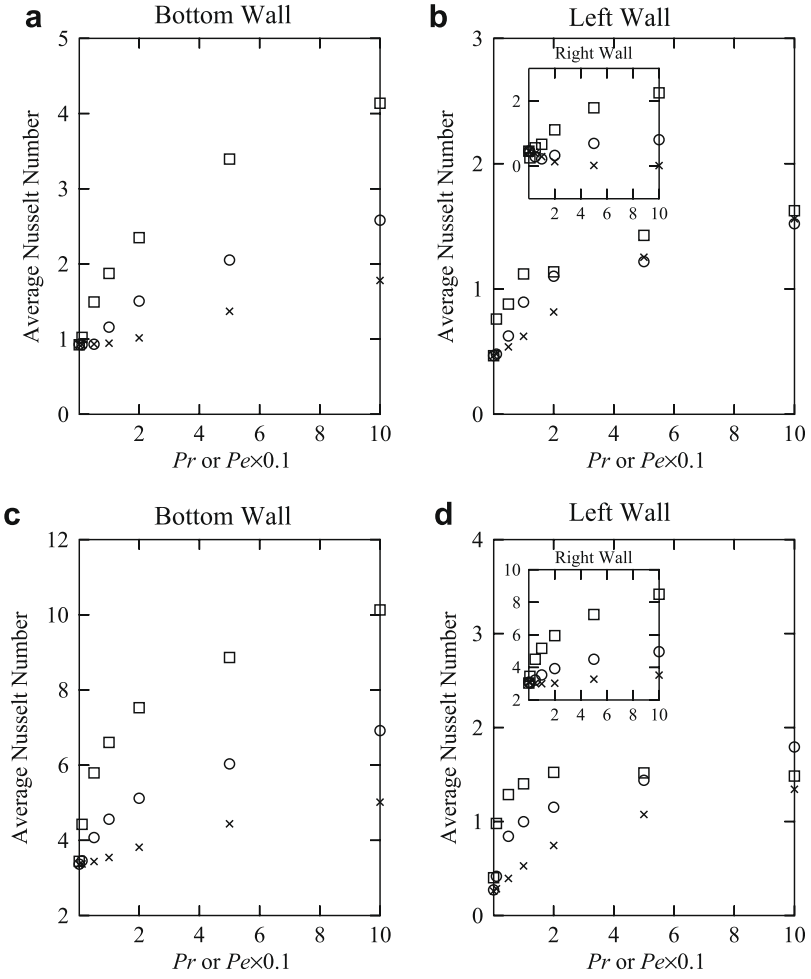


**Fig. 15.** Average Nusselt number vs $Pr$ or $Pe \times 0.1$ for linearly heated side walls (a and b) and linearly heated left wall and cooled right wall (c and d) with $Gr = 10^3; Ri = 10(\times)$, $Gr = 10^4; Ri = 10^2(\circ)$, $Gr = 10^5; Ri = 10^3(\square)$ and $Re = 10$.

that multiple circulation cells are formed with the increase in $Pr$ for moderate Reynolds number in the case of linearly heated side walls. For $Pr = 0.015$ with $Gr = 10^5$ and $Re = 10$, only two circulation cells are formed inside the cavity. As $Pr$ increases to 0.7, three circulation cells are formed inside the cavity. Further increase in $Pr$ to 10, leads to the formation of four circulation cells inside the cavity. On the other hand, only two circulation cells are formed inside the cavity for the case of cooled right wall for identical parameters. The forced convection is found to be dominant for $Pr = 0.7$ with cooled right wall and a secondary circulation cell is found at left corner. Similar effects are observed for $Pr = 10$ at $Gr = 10^5$. The effect of $Re$ has also been studied in the present investigation for fixed value of $Pr$ and $Gr$. The secondary vortex at the top left corner disappears for $Re = 10^2$ due to enhanced motion of the upper lid that drags more fluid from left to right part of the cavity. It is interesting to note that uniform mixing at the center is observed for $Pr = 10$, $Re = 10^2$ and $Gr = 10^5$.

The local Nusselt number for the bottom wall ($Nu_b$) shows that heat transfer rate is equal to one at the left and right edges of the bottom wall for the linearly heated side walls. On the other hand, $Nu_b$ is equal to zero on the left edge of the bottom wall but that increases towards the right edge of the bottom wall in the cooled right wall case. In general, $Nu_b$ is larger at the central regime of the bottom wall due to large temperature gradients. It is also observed that the heat transfer rate along the right wall ($Nu_r$) is larger for the case of cooled right wall as compared to linearly heated side walls especially for larger $Gr$ ($Gr = 10^5$). Both $Nu_l$ and $Nu_r$ show oscillatory behavior for larger $Pr$ and $Gr$ due to presence of multiple circulation cells in the case of linearly heated side walls while only $Nu_l$ shows oscillation in the case of cooled right wall due to presence of secondary circulation near the left wall. The average Nusselt number for the bottom wall ($\overline{Nu_b}$) shows power law variations for $Gr$ with higher $Pr$. On the other hand, both $\overline{Nu_l}$ and $\overline{Nu_r}$ show oscillation and power law variations may not be obtained. It is also observed that $\overline{Nu_b}$ and $\overline{Nu_r}$ are larger at higher values of $Pr$ and $Gr = 10^5$ whereas $\overline{Nu_l}$ is an weaker function of $Gr$ for all $Pr$.

## Acknowledgements

Authors thank anonymous reviewers for critical comments which improved the quality of the manuscript.

## References

[1] O. Aydin, A. Ünal, T. Ayhan, A numerical study on buoyancy-driven flow in an inclined square enclosure heated and cooled on adjacent walls, Numer. Heat Transfer A 36 (1999) 585–599.
[2] C.K. Cha, Y. Jaluria, Recirculating mixed convection flow for energy extraction, Int. J. Heat Mass Transfer 27 (1984) 1801–1810.
[3] J. Imberger, P.F. Hamblin, Dynamics of lake reservoirs and cooling ponds, A. Rev. Fluid Mech. 14 (1982) 153–187.
[4] F.J.K. Ideriah, Prediction of turbulent cavity flow driven by buoyancy and shear, J. Mech. Eng. Sci. 22 (1980) 287–295.

[5] L.A.B. Pilkington, Review lecture: the float glass process, Proc. R. Soc. Lond. 1A314 (1969) 1–25.
[6] R. Schriber, H.B. Keller, Driven cavity flows by efficient numerical techniques, J. Comput. Phys. 49 (1983) 310–333.
[7] M.C. Thompson, J.H. Ferziger, An adaptive multigrid technique for the incompressible Navier–Stokes equations, J. Comput. Phys. 82 (1989) 94–121.
[8] C. Nouar, Numerical solution for laminar mixed convection in a horizontal annular duct: temperature-dependent viscosity effect, Int. J. Numer. Methods Fluids 29 (1999) 849–864.
[9] A. Bejan, Convection Heat Transfer, Wiley, New York, 2004.
[10] M.K. Moallemi, K.S. Jang, Prandtl number effects on laminar mixed convection heat transfer in a lid-driven cavity, Int. J. Heat Mass Transfer 35 (1992) 1881–1892.
[11] A.K. Prasad, J.R. Koseff, Combined forced and Natural convection heat transfer in a deep lid-driven cavity flow, Int. J. Heat Fluid Flow 17 (1996) 460–467.
[12] A.A. Mohamad, R. Viskanta, Effects of upper lid shear on the stability of flow in a cavity heated from below, Int. J. Heat Mass Transfer 32 (1989) 2155–2166.
[13] A.M. Al-Amiri, K.M. Khanafer, I. Pop, Effect of sinusoidal wavy bottom surface on mixed convection heat transfer in a lid driven cavity, Int. J. Heat Mass Transfer 50 (2007) 1771–1780.
[14] A.A. Mohamad, R. Viskanta, Transient low Prandtl number fluid convection in a lid driven cavity, Numer. Heat Transfer A 19 (1991) 187–205.
[15] C.J. Chen, K.S. Ho, Finite analytical numerical solution of heat transfer in two dimensional cavity flow, Numer. Heat Transfer 4 (1981) 179–197.
[16] K. Torrance, R. Davis, D. Gill, D. Gautam, A. Hsui, S. Lyons, H. Zien, Cavity flows driven by buoyancy and shear, J. Fluid Mech. 51 (1972) 221–231.
[17] R. Iwatsu, J.M. Hyun, K. Kuwahara, Convection in a differentially heated square cavity with a torsionally oscillating lid, Int. J. Heat Mass Transfer 35 (1992) 1069–1076.
[18] R. Iwatsu, J.M. Hyun, K. Kuwahara, Numerical simulation of flows driven by torsionally oscillating lid in a square cavity, J. Fluids Eng. 114 (1992) 143–149.
[19] R. Iwatsu, J.M. Hyun, Three dimensional driven cavity flows with a vertical temperature gradient, Int. J. Heat Mass Transfer 38 (1995) 3319–3328.
[20] A.A. Mohamad, R. Viskanta, Flow and Heat transfer in a lid driven cavity with a stably stratified fluid, Appl. Math. Model 19 (8) (1995) 465–472.
[21] V.S. Arpaci, P.S. Larsen, Convection Heat Transfer, Prentice Hall, 1984. p. 90.
[22] A.J. Chamkha, Hydromagnetic combined convection flow in a vertical lid-driven cavity with internal heat generation or absorption, Numer. Heat Transfer A 41 (2002) 529–546.
[23] H.F. Oztop, I. Dagtekin, Mixed convection in two sided lid-driven differentially heated square cavity, Int. J. Heat Mass Transfer 47 (2004) 1761–1769.
[24] E. Papanicolaou, Y. Jaluria, Mixed convection from an isolated heat source in a rectangular enclosure, Numer. Heat Transfer A 18 (1990) 427–461.
[25] T.H. Hsu, P.T. Hsu, S.P. How, Mixed convection in a partially divided rectangular enclosure, Numer. Heat Transfer A 31 (1997) 655–683.
[26] T.H. Hsu, S.G. Wang, Mixed convection in a rectangular enclosure with discrete heat sources, Numer. Heat Transfer A 38 (2000) 627–652.
[27] J.N. Reddy, An Introduction to Finite Element Analysis, McGraw-Hill, New York, 1993.
[28] O.C. Zienkiewicz, R.L. Taylor, J.M. Too, Reduced integration technique in general analysis of plates and shells, Int. J. Numer. Methods Eng. 3 (1971) 275–290.
[29] S. Roy, T. Basak, Finite element analysis of natural convection flows in a square cavity with non-uniformly heated wall(s), Int. J. Eng. Sci. 43 (2005) 668–680.
[30] T. Basak, S. Roy, A.R. Balakrishnan, Effect of thermal boundary conditions on natural convection flow in a square cavity, Int. J. Heat Mass Transfer 49 (2006) 4525–4535.
[31] G.K. Batchelor, An Introduction to Fluid Dynamics, Cambridge University Press, 1993.
[32] M.M. Ganzarolli, L.F. Milanez, Natural convection in rectangular enclosures heated from below and symmetrically cooled from the sides, Int. J. Heat Mass Transfer 38 (1995) 1063–1073.